A frequency dependent drag coefficient on the motion response model of a hybrid STC wind-wave energy converter

Master Thesis

L.S. Kohlmann

TU Delft

A frequency dependent drag coefficient on the motion response model of a hybrid STC wind-wave energy converter

Master Thesis

by

L.S. Kohlmann

Student number: 4225953
Project duration: March 1, 2019 – December 13, 2019
Thesis committee: Dr. ir. P. Wellens, TU Delft
Ir. P. Xu TU Delft

This thesis is confidential and cannot be made public until December 13, 2019.

TU Delft

Abstract

The vertical viscous drag force acting on a heaving cylinder with flat and hemispheric bases is investigated by means of an experiment, a linear and a nonlinear analytic model. Viscous effects create a significant uncertainty in estimating the motion response of oscillating cylinders in waves of different frequencies.

Forced oscillation tests are compared with a linear analytic model and approximated with a nonlinear model to quantify the viscous drag force for a range of oscillating frequencies. The results asses the behaviour of the drag coefficient, C_D, to be used for calculating the drag force. The main interest of this study is to improve the estimation of the motion response of floating hybrid wind-wave energy converters.

The hydrodynamic parameters, added mass and radiation damping, used in the linear model are obtained with the boundary element method (BEM) solver NEMOH. The same parameters are obtained from the experiment for comparison. Near the natural frequency of the geometries the linear model underestimate the forces due to the absence of a nonlinear viscous drag term.

The time traces of the force measurement around the natural frequencies show period doubling behaviour which can be described by the quadratic velocity term in the drag force calculation. By applying the least-squares optimization method on the obtained data, optimal variables in the fit-function including the quadratic drag term are found. The results show the drag coefficient, C_D, is changing over the frequency of oscillation.

The vertical drag force is frequency dependent and therefore important to consider when calculating the motion response of wave energy converters.

Highlights

- Development of a new approach by examining the vertical, instead of in-line, drag force component of floating oscillating bodies.
- Experimental generation of data.
- Assessment of a linear numerical method for obtaining hydrodynamic parameters.
- Clear description of the vertical viscous drag force behaviour over the frequency domain.
- Performance study on analytic models describing the viscous drag force.
- Established relationship of the drag coefficient over the frequency of oscillation.

Contents

Nomenclature

Abbreviations

$B.L.$	Boundary layer
BEM	Boundary Element Method
BVP	Boundary Value Problem
FFT	Fast Fourier Transform
KC	Keulegan-Carpenter number
PA	Point Absorber
PTO	Power Take Off
Re	Reynolds number
STC	Spar Torus Combination
WEC	Wave Energy Converter

Arabic symbols

$\vec{U}$	Flow velocity vector	m/s
a	Added mass	kg
A_w	Waterline area	m^2
b	Damping coefficient	Ns/kg
c	Restoring stiffness	kg/s^2
C_D	Drag coefficient	–
D	Cylinders diameter	m
F_a	Force amplitude	N
F_D	Drag force	kg
F_z	Excitation Force	N
g	Gravitational acceleration	m/s^2
H	Draft cylinder without appendage	m
k	Mean roughness height	μm
m	Mass of cylinder	kg
P	Mass force	N
p	Pressure	N/m^2
r	Radius of cylinder	m
T	Draft	m

t	Time	s
T_c	Water temperature	$°C$
T_ω	Period of oscillation	s
u_a	Flow velocity	m/s
v	Logarithmic decrement	–
V_r	Reduced velocity	–
z	Vertical displacement	m
z_a	Amplitude of oscillation	m

Greek Symbols

λ	Wave length	m
λ_F	Froude scaling factor	–
ν	Kinematic viscosity	mm^2/s
ω	Frequency of oscillation	rad/s
Φ	Velocity potential	m^2/s
ρ	Density fluid	kg/m^3
τ	Shear stress	N/m^2
ε	Phase	rad

1 Introduction

Everyone is aware of the earth's changing climate. It is generally acknowledged that people have a negative impact by incessantly consuming non-renewable energy sources. In 2015, the United Nations assembled a list of 17 sustainable development goals to stimulate action in areas of importance for humanity and the planet [4]. In the search for cost-efficient clean energy solutions, this master thesis will focus on the dynamic response of a hybrid wind-wave energy converter. In this way, a contribution can be made in the process of reaching three of the goals; Clean affordable energy, climate action and conservation of life below water. This chapter will provide a background to the problem, the research question and an outline of the report.

1.1. Background

Offshore, ground-based, wind farms are becoming economically viable and are already an important contributor in the energy transition striving to a more sustainable world. But despite an incredible 70% total installation cost reduction between 2013 and 2022, subsidies are still necessary to bring the energy to shore [15].

A way to decrease the overall costs is to increase the efficiency of a farm. Wind is a source that creates waves, so where there is wind consequently there are waves. Therefore, the attention is drawn to combine wind and wave energy devices in offshore areas. Wave energy devices are studied since the 1970s but have proven to be unattractive for commercial use [22]. A large contributor to the high costs is the electrical grid that needs to be installed. Hybrid solutions can use the same infrastructure which increases the overall efficiency of wind farms and contribute to the viability of wave energy devices. In a feasibility study of van Riet, different hybrid solutions are evaluated [17]. The Spar-Torus combination (STC) , figure 1.1, in this research has an estimated 10-15% higher energy production compared to a floating spar wind turbine without a wave-energy converter (WEC). This extra yield is caused by a combination of the increase in wind energy production of 6% due to extra stability of the spar delivered by the WEC and the addition of energy absorbed by the WEC itself [14]. These are encouraging indications for further analysis of the system.

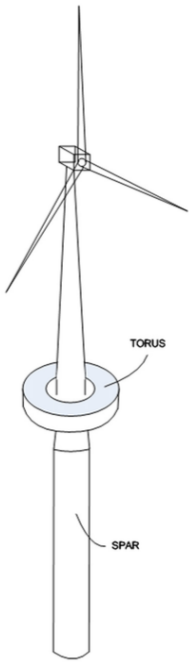

Figure 1.1: Sketch of a wind-wave energy converter [14]

To optimize the energy uptake of the dynamic system, its behaviour in wind and waves has to be known. In several researches conducted in Norway the dynamic response in operational conditions and in survival modes are investigated to give an insight in the feasibility of the design [12] [13] [14] [21]. The results, as men-

tioned earlier, are positive and further research into the operational dynamic response is desirable. Correct prediction of the motion of the Torus in different sea states is required to optimize the stiffness settings of the power-take-off (PTO) that translates the kinetic energy of the Torus to electric power. An important factor in the motion behaviour of the torus is the damping. Next to linear wave-damping, viscous effects contribute to the total damping in the system. Viscous effects are challenging to model as they behave non-linear, so often they are estimated using a drag force formulation containing an empirical determined drag coefficient. Despite the frequency dependent characteristics of the drag coefficient, many researchers investigating the motion of WECs treat the drag coefficient like a constant [5] [9] [14] [21].

1.2. Problem statement

The dynamic response of a STC is first studied in 2013 by M.J. Muliawan et al [14]. Thereafter, several papers are written on the subject, focussing primarily on extreme responses in survival mode conditions. A detailed study into the hydrodynamics of the model in operational sea states can provide new insights in the behaviour of the torus motion and help optimizing the system for maximum energy uptake.

An assumption that is commonly used for describing the viscous drag of a geometry in an oscillating flow is the value of the drag coefficient in the drag force formulation. In an early study, the dependency of the drag coefficient on different parameters is investigated for a fixed cylinder in oscillating flow. Important parameters are the Keulegan-Carpenter number (KC) , Reynolds number (Re), relative roughness (k/D) and the reduced velocity (V_r) if current is involved [18]. This research investigated, in particular, the in-line force on a fixed cylinder in current and waves. The driving force of a point absorber(PA) WEC is the orbital movement of the incoming wave. The flow around the PA is dependent on the frequency of the wave and the response of the PA. Because the direction and speed of the flow changes during the motion, the value of the drag coefficient is a considerable uncertainty. Nevertheless, the results of the research of Sarpkaya and Storm [18] are commonly used as source for the determination of the drag coefficient for wave energy devices.

The focus of this study will be on the frequency dependency of the drag coefficient for heaving rigid bodies in waves to improve motion response calculations. The main research question that is derived from this challenge is as follows:

Can a frequency dependent drag coefficient improve the accuracy in estimating the damping response of a STC hybrid wind-wave energy converter?

To support this research question the following sub-questions are formulated which will be investigated to provide an answer to the main question:

- What is the behaviour of the viscosity on the damping of a buoy oscillating at different frequencies?
- Is there an analytic model, that includes a drag coefficient, that can describe the viscous damping?
- How does the new model compare to existing methods?

1.3. Methodology

To give answers to the sub-questions and therewith to the main research question, an overview of the steps is given. The thesis started with the creation of a theoretical framework. This framework will function as a basis of the considered system and flow physics. Due to the complexity of the flow, experimental data is collected to capture the non-linear viscous damping effects. Experimental tests are conducted in the towing tank of the TU Delft's faculty of Maritime Engineering. An analytical model is created based on linear potential flow theory so in combination with the experimental results the the non-linear part of the damping can be quantified. The data is analysed to see if a frequency dependent drag coefficient could be found to improve motion calculations of the WEC.

2

Literature review

WECs aim to respond at their natural frequency in the sea-state they will be deployed in. This is because the amount of kinetic energy that can be harvested has a maximum around the natural frequency. In this region, damping has a high influence on the response of the system. To find the response of the heaving buoy, first the physical phenomena have to be understood. In this chapter the different loads acting on a buoy in waves are elaborated and a theoretical description is given of the linear and nonlinear analytic system approach. The chapter will end with the state of the art considering the nonlinear viscous drag determination which will enlighten the knowledge gap that is tried to narrow with this thesis.

2.1. Environmental loads

In this section the situation of the system is sketched and the loads that are present in the real-life situation are explained. The point absorber is simplified as a cylindrical buoy.

Axis convention
For this research an earth-bound coordinate system is used where the x- and y-axis are located on the still water surface, S, and the z-axis is pointing upwards, see figure 2.1. The rigid body, the buoy, is constrained in all directions except heave which corresponds to translations along the z-axis.

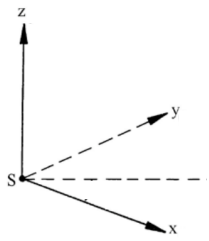

Figure 2.1: Axis agreement

Loads
Waves initiate oscillating pressures on the cylinder. Two kinds of forces are caused by waves on a cylinder, **Inertial** forces and **Drag** forces. Inertial forces contain: 1. The Froude-Krylov force; the pressure difference caused by the undisturbed wave, 2. The diffraction force; the force corresponding to the deflection of fluid particles due to the presence of a structure, 3. The radiation force; caused by the (heaving) motion of the body. In figure 2.2 the three forces are schematically visualised where z is the distance to the free surface, p is the pressure and λ the incoming wave. All the inertial forces can be derived from potential flow theory. The drag forces contain: 1. Form drag; flow separation due to normal stresses, 2. Friction drag; shear stresses creating boundary layers in the fluid around the body. In figure 2.3 the drag force components are schematically visualised where u is the flow velocity, τ the shear stress and $B.L.$ stands for boundary layer.

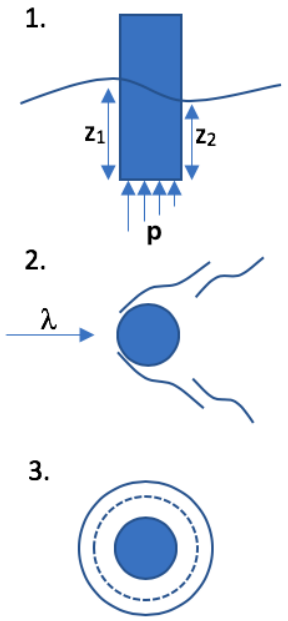

Figure 2.2: 1. Froude-Krylov 2. Diffraction 3. Radiation

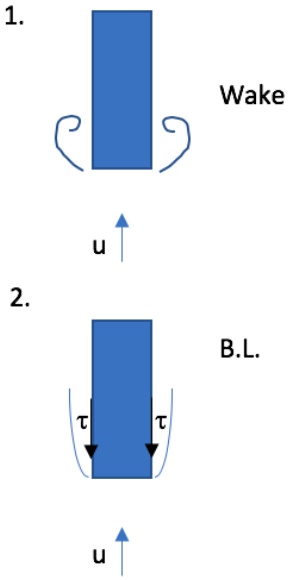

Figure 2.3: 1. Form drag 2. Friction drag

The drag forces are harder to calculate as they behave nonlinear and are dependent on a variety of flow and geometry parameters. As earlier stated, important, dimensionless, parameters that indicate the behaviour of the viscous drag are the Reynolds number (2.1) and the Keulagan-Carpenter number (2.2). The Reynolds number indicates the flow regime ranging from a laminar (small drag) to a fully turbulent flow (large drag), see figure 2.4. The KC-number indicates the importance of the drag force related to the inertial forces. In engineering applications the following rule is followed: When $KC < 1$, drag forces can be neglected, when $KC >> 1$, drag forces are important. For KC-values in between, both drag and inertia forces have to be considered [11].

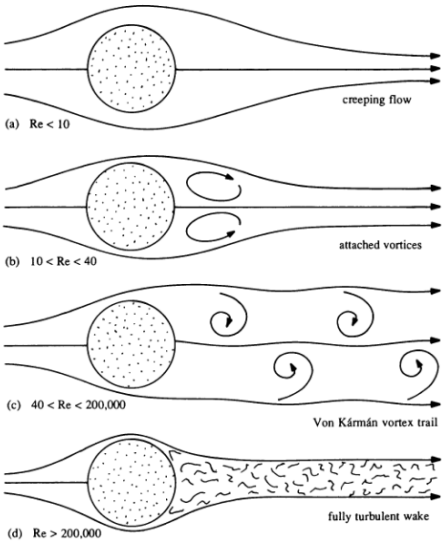

Figure 2.4: Flow around a circular cylinder for different Reynolds numbers [7]

$$Re = \frac{u_a \cdot D}{\nu} \tag{2.1}$$

$$KC = \frac{u_a \cdot T_\omega}{D} \tag{2.2}$$

Where:

u_a = Flow velocity [m/s]
D = Diameter of cylinder [m]
T_ω = Period of oscillation [s]
ν = Kinematic viscosity [mm^2/s]

For this study, the drag forces are of interest as they have a significant contribution to the damping of the system. To capture the drag forces two approaches are considered: an experiment and an analytic model.

2.2. System approach

To be able to asses the viscous damping, the WEC is simplified as a cylinder. Still water tests have shown to be an approved way to capture the hydrodynamic loads on an oscillating cylinder. This study uses a new advanced design method by looking only to the characteristics of the drag force in vertical direction (see figure 2.5) . To capture this force, two experiments are performed: A forced motion test, to find the excitation force needed to oscillate the cylinder at different frequencies, and a free decay test, to capture the time needed for the cylinder to get back to its equilibrium after an initial displacement is given. To describe the tests with an analytical model, first, a linear approach is considered.

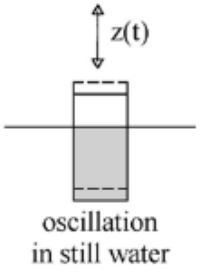

Figure 2.5: Cylinder oscillating in vertical direction

2.2.1. Linear model

The free body diagram for a free oscillating cylinder is illustrated in figure 2.6. This sketch shows two positions of the cylinder, one at its equilibrium and one with a positive offset. A body fixed axis is used with its origin in point *O*. If all the hydrodynamic forces are added, Newtons law of motion can be derived. In equation 2.3 this derivation is shown [7].

$$\begin{aligned} m\ddot{z} &= \text{sum of all forces on the cylinder} \\ &= -P + pA_w - b\dot{z} - a\ddot{z} \\ &= -P + \rho g(T-z)A_w - b\dot{z} - a\ddot{z} \end{aligned} \tag{2.3}$$

Where:

m	= Mass of the cylinder [kg]
A_w	= Waterline area [m^2]
T	= Draft [m]
$P = mg$	= Mass force [N]
a	= Added mass [kg]
b	= Damping coefficient [Ns/kg]
z	= Vertical displacement [m]

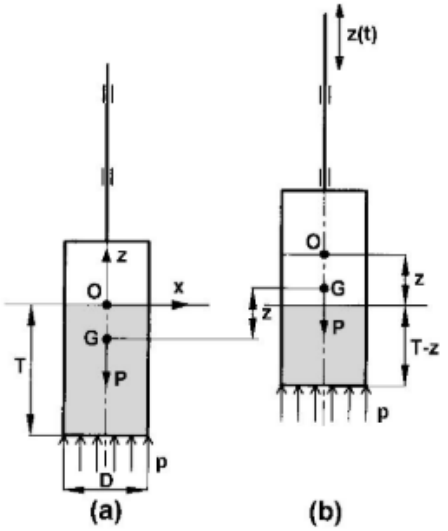

Figure 2.6: Free body diagram of an oscillating cylinder [7]

If the mass force is substituted with Archimede's law where $P = \rho g T A_w$, the final motion equation for the free decay test can be represented by equation 2.4.

$$(m+a)\ddot{z} + b\dot{z} + cz = 0 \tag{2.4}$$

Where:

$c = \rho g A_w$ = Restoring stiffness [kg/s^2]

The added mass is described as the mass of the fluid around the cylinder that is set in motion due to the acceleration of the body. The damping in the equation is the only term that extracts energy from the system which causes the cylinder to get back to its equilibrium after an initial displacement is given. In the linear equation of motion only radiation forces contribute to the damping. During a forced motion test the displacement, velocity and acceleration are imposed and therefore known, see equation 2.5. The required excitation force that is needed to follow the imposed path is measured to give a time trace of the force amplitude. The system can be schematically visualised by a single mass-damper-spring system, figure 2.7. The linear motion equation for the forced motion test is described by equation 2.6.

$$\begin{aligned} z &= z_a \sin \omega t \\ \dot{z} &= z_a \omega \cos \omega t \\ \ddot{z} &= -z_a \omega^2 \sin \omega t \end{aligned} \tag{2.5}$$

$$(m+a)\ddot{z} + b\dot{z} + cz = F_z(t) \tag{2.6}$$

Where:

z_a = Amplitude of oscillation [m]
ω = Oscillation frequency [rad/s]
t = Time array [s]
F_z = Recquired excitation force [N]

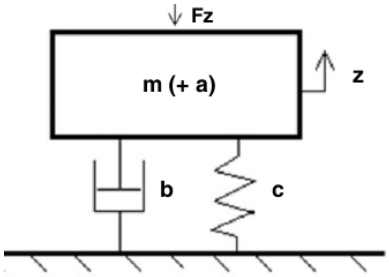

Figure 2.7: Mass-spring-damper system

The linear motion equations consist of three terms: the inertia term (m+a) corresponds with the acceleration, the damping (b) with the velocity and the restoring stiffness (c) with the displacement. At certain oscillating frequencies the motion equation is governed by one of the three terms which is caused by the different phases of the displacement (0), velocity ($-\pi/2$) and acceleration ($-\pi$). At the natural frequency of the system the restoring stiffness term has the same amplitude as the inertia term so they cancel out and only the damping term is left. In figures 2.8 and 2.9, the dominant regions and the time traces of the displacement, velocity and acceleration are illustrated.

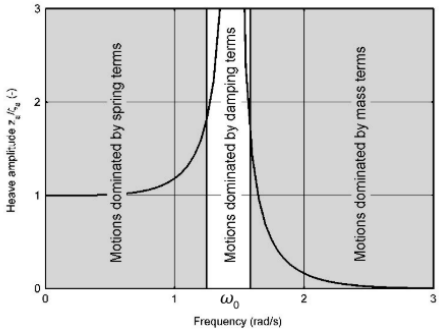

Figure 2.8: Region of dominance in motion equation [7]

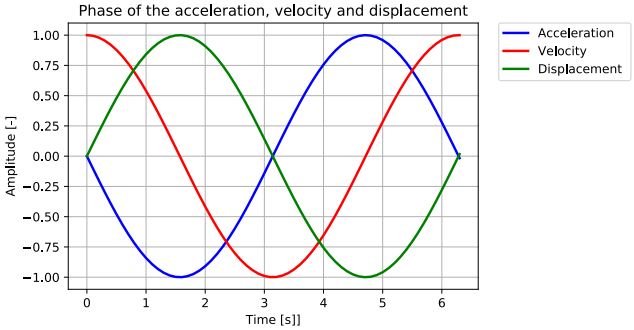

Figure 2.9: Time trace of the displacement (z), velocity ($\dot{z}$) and acceleration ($\ddot{z}$)

To study the nonlinear behaviour of the damping term at different frequencies the key is to isolate it. Only the added mass and linear damping terms are unknowns in the linear motion equation. The added mass and linear damping coefficient can be calculated with potential flow theory, where it is assumed that the fluid is inviscid, irrotational and incompressible. In this research a 3D BEM solver is used to find the added mass and damping coefficients.

Now the linear analytic model is described, the nonlinear viscous drag term can be isolated by comparing it with the results of the tank test. The difference between the tank test and the linear analytic model is assumed to be caused by the viscous effects explained in the previous section. Because of the complexity of this flow due to its nonlinear behaviour, many researches looked into ways to estimate the forces caused by these effects by means of an empirical determined analytic model. In the next section, 2.2.2, a detailed elaboration on the established drag force formulation is presented and other, state of the art, methods in estimating the nonlinear viscous forces are explained.

2.2.2. Nonlinear viscous drag

During the last decades many experiments are conducted with cylinders in flow and have proven that the viscous drag force is proportional to the flow velocity squared , $\dot{z}^2$, and the diameter of the cylinder [7]. In equation 2.7, the drag force formulation for a cylinder in oscillating flow is stated. The absolute value of the velocity is considered to correct the sign, as in oscillating flow this changes direction during the cycle. In the equation the drag coefficient (C_D) is determined empirically. In this section, the focus will be on the determination and behaviour of the drag coefficient.

$$F_D(t) = \frac{1}{2}\rho C_D D u_a^2 \cdot \cos(\omega t) \cdot |\cos(\omega t)| \tag{2.7}$$

The drag coefficient is influenced by various parameters like, roughness, shape, flow velocity and viscosity of the fluid. Many studies examined the drag coefficient by experiments in oscillating flow for geometries of various shapes, sizes and roughness [8] [18] [20]. As a result of the experiments relations between the drag coefficient versus the Reynolds number, and versus the Keulegan-Carpenter number are established. In this research only smooth cylinders are considered.

In figure 2.10 the drag coefficient for a cylinder are related to the Reynolds number and the KC-number. From this figure an indication of the drag coefficient could be obtained. In this figure $\beta = Re/KC$.

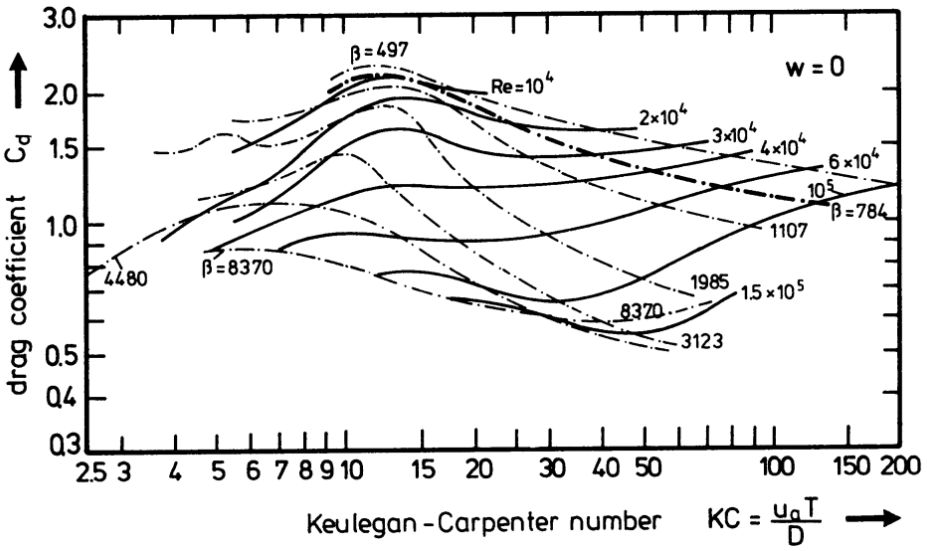

Figure 2.10: Drag coefficient related with the KC number for flow around a smooth cylinder at different Reynolds numbers[18]

As can be seen, the value of the coefficient ranges from 0.5 - 2.5, depending on the Reynolds number or KC number. It is important to note most of the researches consider a cylinder in-line with the oscillatory flow as they were meant to estimate wave forces on cylindrical foundations of offshore structures. One study is found that did not assume the drag coefficient for a PA WEC.

In a research of A.S. Zurkinden et al. [23] the drag coefficient is calculated from an experimental study for a hemispheric point absorber, the wave-star [2]. This point absorber considers both pitch and heave so a horizontal (C_D^h) and vertical (C_D^v) drag coefficient is present. To evaluate the drag coefficient, a forced oscillation test in still water is performed for different frequencies and stroke amplitudes. The obtained values of the drag coefficients are illustrated in figure 2.11. Assumed is that 10 frequencies are tested at 4 different amplitudes, starting left with the largest amplitude.

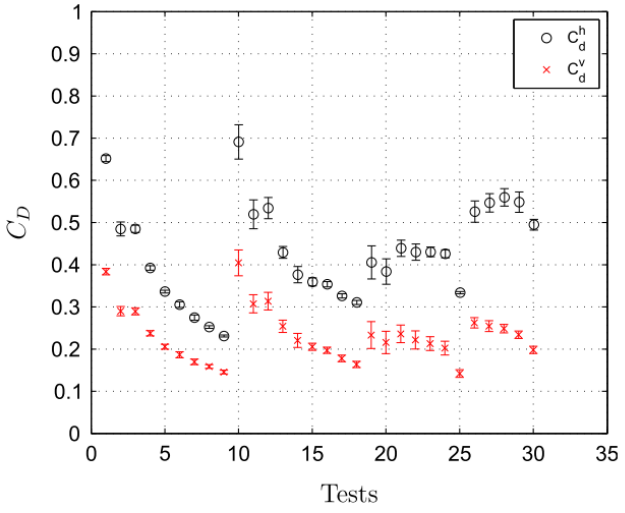

Figure 2.11: Vertical drag coefficient (red) and horizontal drag coefficient (black)

Despite the unclear description of the test frequencies and amplitude, the results shows a frequency dependency of the drag coefficient. Furthermore, if the values are compared to the values in figure 2.10, no correlation can be found, independently of the KC-number value. To conclude the findings, many uncertainties

are still present considering the value of the drag coefficient however, many researches use the information of the established relations.

This thesis takes a step into clarifying the behaviour of the drag coefficient for a heaving point absorber wave energy-converter in the vertical direction. Especially the influence of the frequency around the natural frequency of the system is of interest as this is the design operation condition for wave energy converters. To get a feeling of the viscous drag behaviour, the cylinder in this research is tested with two different bottom shapes: a flat bottom and a hemispheric bottom. The viscous effects are expected to be larger for the flat bottom cylinder as this geometry has sharp edges where flow separation occurs. The tank test result is compared with the linear analytic model and the difference is fitted with a least-squares method.

2.3. Concluding remarks

In this chapter, the physics of the problem are explained and methods to analyse the system are elaborated. Furthermore, literature is reviewed on current approaches towards estimating the drag coefficient for bodies in oscillating flow. Based on this information, three statements are listed which describe the missing knowledge which is related to this thesis:

- The vertical drag coefficient for oscillating cylinders is still a large uncertainty for estimating the non-linear viscous drag force.
- Little information is available on time trace characteristics at different frequencies for a heaving cylinder.
- A clear view of the frequency dependency of the drag coefficient for oscillating cylinders in the vertical direction has not been found.

3

Experimental method

The goal of the experiment is to capture all the hydrodynamic loads on a heaving cylinder with two different bottom shapes, including the loads that corresponds to the viscous flow phenomena. Together with the linear analytical model the nonlinear forces can be separated and quantified. With forced motion tests the force needed at each heaving frequency can be measured. From this data a first analysis can be made to obtain the force amplitudes and hydrodynamic coefficients, added mass and damping.

Next to the forced motion tests, a free decay test for the two geometries at three different amplitudes is performed under the same circumstances. From these results the damping time and natural frequency of both geometries is captured which can help sorting out the relations between shape and non linear effects on damping.

Highlights chapter 3

- Explanation of the experimental set-up and overview of test programme.
- Illustration of the raw measurement results and post-process methods to create useful data.
- Determination of the hydrodynamic parameters from the experimental results.
- Influence of the shape of the geometries on the damping time in the free decay test.

3.1. Model Description

For the tank tests two geometries are used: a cylinder with a flat bottom and a cylinder with a hemispheric bottom which from now on will be referred to as cylinder and hemisphere respectively. In this section the dimensions of the geometries and the way they are created is elaborated together with the tank dimension and set-up for the two tests. In table 3.1 the constant variables are listed. Only slight changes in water temperature are measured and therefore the changes in water density and kinematic viscosity are assumed negligible. A Froude scaling factor of 0.13 is used so the natural frequency of the test geometries corresponds to the frequency of the highest energy peak in the Jonswap spectrum [6].

Table 3.1: Constants of the experimental model

Constant values of experimental model

Description	Symbol	Value	Unit
Water density	ρ	1000	kg/m^3
Water temperature	T_c	20	$^\circ C$
Water kinematic viscosity	ν	1.004e-6	m^2/s
Draft cylinder (no appendage)	H	0.41	m
Diameter cylinder	D	0.197	m
Restoring stiffness	c	299.014	kg/s^2
Mass (incl appendage)	m	14.05	kg
Scaling factor	λ_F	0.13	-

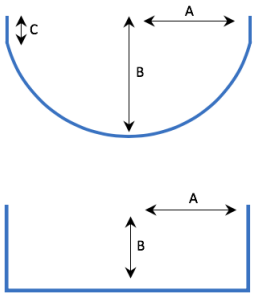

Figure 3.1: Schemetic drawing of appendages

Table 3.2: Dimensions of the appendages

	Dimensions [cm]		
	A	B	C
Hemisphere	9.85	10	1.726
Cylinder	9.85	6.84	-

3.1.1. Geometries

For both the free decay and forced motion test two existing cylinders are used with identical dimensions. The hemisphere that needed to be attached on the bottom of the cylinder had a larger radius (10 [cm]) than the cylinder. To have a smooth transition between the cylinder and the hemisphere it is decided to sand the sides of the hemisphere. The consequence is a slight change in volume and shape which is taken into account throughout the rest of the research. To have valuable results the displacement of both the cylinders, with and without hemisphere, has to be the same. Therefore a cylinder is made with the same volume as the hemisphere. In table 3.2 the dimensions of the two appendages are listed.

In figure 3.2 the two cylinders with the appendages are illustrated.

Figure 3.2: Pictures of the two test geometries

3.1.2. Tank setup

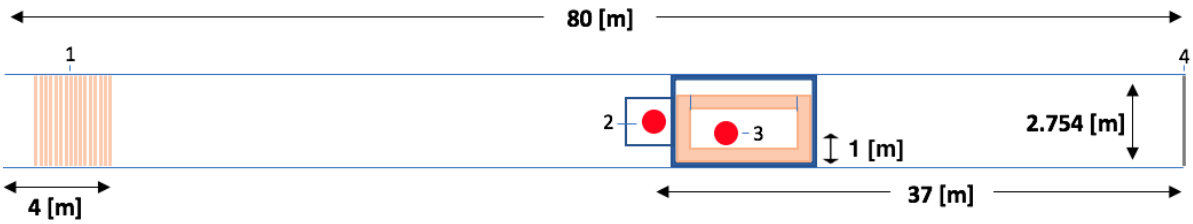

Figure 3.3: Dimensions of towing tank and top-view of the test set-up

The tests are conducted in the small towing tank at the faculty of Maritime Engineering. The dimensions of the towing tank are shown in figure 3.3. The location of the two different tests is different due to the fact that

the free decay test is not positioned in de middle of the width of the towing wagon. The numbers 1-4 indicate the following: 1 The beach, 2 Forced motion test, 3 Free decay test & 4 The wave maker. The forced motion tests are all positioned at a distance of 37 meters from the wave maker to maximise the reflection time of the radiated wave with the wave maker. At low frequencies (0.3 [Hz]) this means a clean run time of 23 seconds before the reflection is back at the buoy. The reflection of the sides of the tank are also considered in the simulation and will be discussed in chapter 4. The water depth with the forced motion test is 1.2 [m].

Forced motion test:

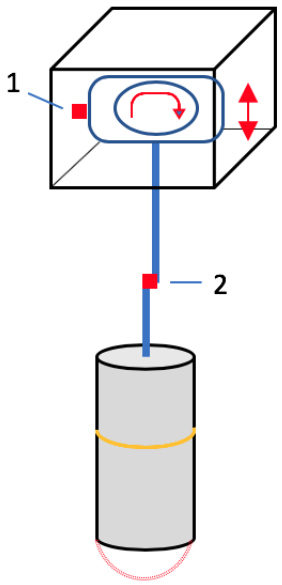

Figure 3.4: Schematic drawing of forced motion set-up.

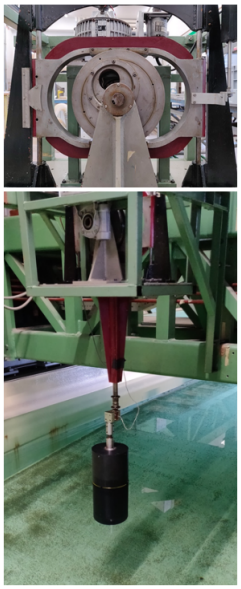

Figure 3.5: Pictures of the forced motion set-up.

In figure 3.4 a schematic visualisation of the forced motion test set-up is illustrated. The sensors are indicated with numbers: 1 = displacement sensor and 2 = force sensor. Next to it, the real situation is shown in figure 3.5. The oscillation is powered by an electric motor which has a transmission ratio of 1440:1, motor rpm to frequency of oscillation in [Hz]. The controller of the motor runs on a 50 [V] power supply and is attached to a PC that tells the controller how much power he needs to deliver to the motor so the velocity up and down is constant. The amplitude of the oscillation can be adjusted from 0 to 6 cm. The force sensor (wheatstoner bridge) has a sensitivity of 100 [N] and is connected to an analogue conditioner which amplifies the signal between -10 and 10 [V]. Next, the signal is passed on to a data acquisition station with a 100 [Hz] second order low pass filter after it continues to the PC which has a sample rate of 1000 [Hz] so aliasing will not occur. The distance sensor is connected to a pod meter where the signal is balanced at 0 when the cylinder is located at the correct waterline. Due to mechanical friction of the oscillator the signal is noisy with large peaks at the moment the direction is changed from up to down and vice versa. The height of the oscillator is fixed which means that the depth of the tank decides where the waterline will be. To have a corresponding displacement with the free decay test the water depth is set to 1.2 [m] and the weight of the cylinder has to be 14.05 [kg]. The maximum speed of the oscillator is fixed at 1500 [rpm], so a frequency of oscillation of 1.042 [Hz].

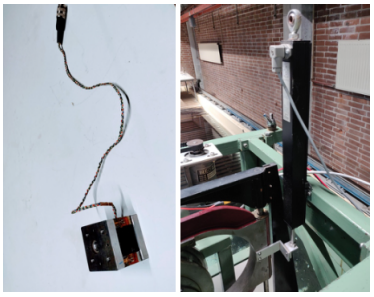

Figure 3.6: Force (l) and distance (r) sensors

Free decay:

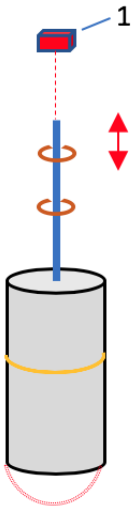

Figure 3.7: Schematic drawing of free decay test set-up.

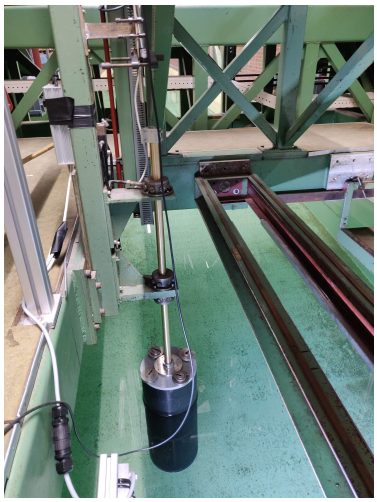

Figure 3.8: Picture of the free decay test set-up.

In figure 3.7 a schematic drawing of the free decay test set-up is shown. The cylinder is attached to a metal pipe that is running through two air bearings. These air bearings are connected to pressurised air of 5 [bar]. Above the metal pipe a laser distance sensor, indicated with the number 1, is attached to the wagon and pointed to the top of the metal pipe, see figure 3.9. The sensor amplified the signal itself so it could be connected directly to the data acquisition station before it was connected to the PC. The free decay test position is slightly off the middle of the width of the tank. In the result this has to be considered as the reflection of the radiated waves will have another phase. A picture of the set-up can be seen in figure 3.8. The water depth was increased to 1.4 [m] because the length of the pipe was too short to go through the highest air bearing if the amplitude of oscillation was 10 [cm]. The buoy that is used for the free decay test is not the same as used during the forced motion test although the radius is exactly the same, the weight is not. To overcome this, additional weights are added to the buoy to have the exact same weight during both tests (14.05 [kg]).

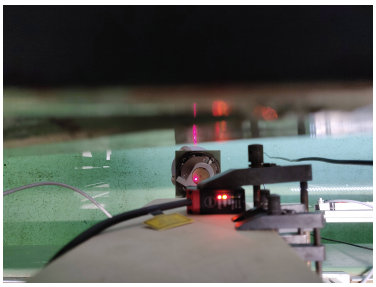

Figure 3.9: Free decay distance sensor

3.2. Method

Now the set-up is defined, the way the tests are performed is elaborated in this section. The test matrix will be presented and the strategy to obtain the data of most interest is explained.

Forced motion test:

During the forced motion test 3 signals are measured; time [s], distance [cm], force [N]. The goal of the test is to obtain the data of the force at different frequencies. Especially the natural frequency of the system is of interest as this is the region where the damping term dominates the motion. The runs are executed with the help of a test matrix. A standard program is made for the first 8 runs for every geometry. After these runs a first view of the location of the natural frequency is obtained and further runs can serve as a convergence study towards the real natural frequency. To be able to see discrepancies in the data, the standard program is set-up in a way that after a low frequency run a high frequency run will be performed and vice-versa. Before every run a zero measurement is conducted to see if the water is calm enough to perform a run. The time between runs differs between 2 - 20 minutes, depending on the frequency, the amplitude and if tests are going on in the tank aside. For both geometries three amplitudes are tested at 0.28 [cm], 2 [cm] and 5 [cm]. This is because at smaller amplitudes the physical phenomena behave more linear so a trend can be seen in what degree the non-linear effects increase over the amplitude. The tests at 5 [cm] have more runs as this is the amplitude

where the (non-linear) effects are expected to be the largest. All the measurements have a run time of 60 [s]. A checkrun is performed at the natural frequency to see if the data is reliable. At the tests with amplitude 5 [cm] a reflection run is done to see what influence this has on the data. Most of the runs are performed with an amplitude of 5 [cm] with an exception at the natural frequency where the run is performed at three different amplitudes.

Table 3.3: Program Forced Motion test

Test matrix

	Amplitude [cm]	Frequencies (standard) [Hz]								Frequencies (convergence study) [Hz]										Natural Frequency [Hz]
Cylinder	5.00	0.3	1.0	0.4	0.9	0.5	0.8	0.6	0.7	0.65	0.75	0.675	0.6875	0.6625	0.68125	0.684375	0.678125	0.625	0.725	0.678125
	2.00									0.678125	0.65	0.75	0.725	0.6625	-	-	-	-	-	
	0.28									0.678125	0.65	0.75	0.675	0.725	0.6625	-	-	-	-	
Hemisphere	5.00									0.65	0.75	0.675	0.725	0.6875	0.7125	0.69375	0.70625	0.696875	0.703125	0.7
	2.00									0.65	0.75	0.675	0.725	0.6875	0.7125	-	-	-	-	
	0.28									0.65	0.75	0.675	0.725	0.6875	0.7125	-	-	-	-	

Free decay:

For the free decay test only two signals are measured; time and distance. The goal of this test is to obtain the time it takes for the buoy to come to the static state after it is displaced a certain distance from it's equilibrium. The tests are conducted at three different amplitudes; 10, 7.5 and 5 [cm]. The initial displacement is obtained by pushing the buoy down until it reached the desired distance set by three wooden sticks that corresponded to the amplitudes. The test matrix is shown in table 3.4. Before every run a zero measurement is performed and a minimum of two check runs at the same amplitude are conducted to see discrepancies.

Table 3.4: Program free decay test

Test matrix

	Amplitude [cm]		
Cylinder	10	7.5	5
Hemisphere	10	7.5	5

3.3. Results

In this section, the results of the test measurement are presented divided in four subsections: Force, added mass and damping, free decay and finally the uncertainties. The used equation in this section are all obtained from the book "Offshore Hydrodynamics" by J. Journee and W. Massie [7].

3.3.1. Force

The sample frequency of the force measurements was 1000 [Hz]. In figures 3.10 and 3.11 the raw signal and filtered signal are plotted for the measurement at an oscillation of 4.26 [rad/s] for the cylinder. A Butterworth filter design is used with a cut-off frequency at 2π [rad/s]. In section 3.4.1 a sensitivity analysis is conducted for the measurements at the natural frequency of the geometries to see the influence of the filter on the different parameters.

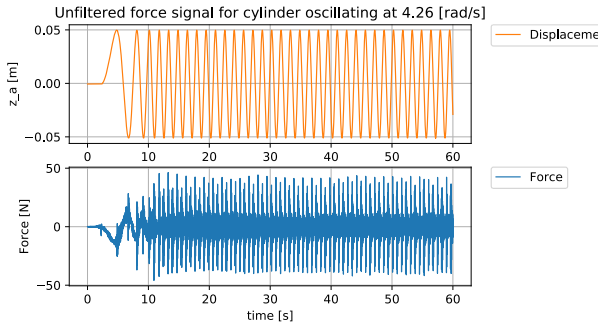

Figure 3.10: Unfiltered force signal

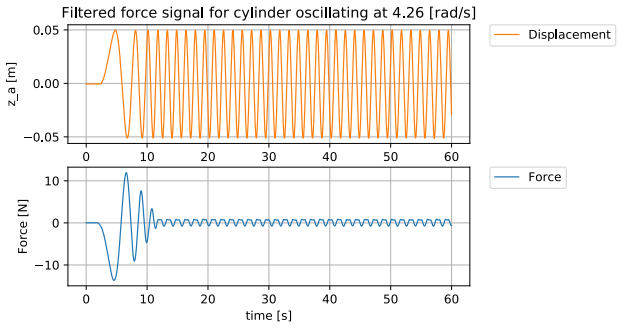

Figure 3.11: Filtered force signal

As can be seen, the motor of the oscillator needs time to reach the desired frequency. Therefore, the first 18 seconds of each measurement are not taken into account during the analysis of the results. For the first analysis, the force amplitude, added mass and damping coefficients from each measurement are acquired by applying a linear sin fit on the filtered data. This method gives an accurate impression on the force peaks but does not cover nonlinear viscous effects that are visual in the time traces close to the natural frequency, as can be seen in figure 3.12. In chapter 5 the nonlinear analysis will be elaborated in detail. In figure 3.13 a graph is illustrated to indicate the force amplitudes measured at each frequency for the cylinder and hemisphere with a motion amplitude of 5.04 [cm]. The natural frequencies that correspond to the cylinder and hemisphere are respectively; $\omega_{0_{cyli}}$=4.26 [rad/s] and $\omega_{0_{hemi}}$=4.40 [rad/s].

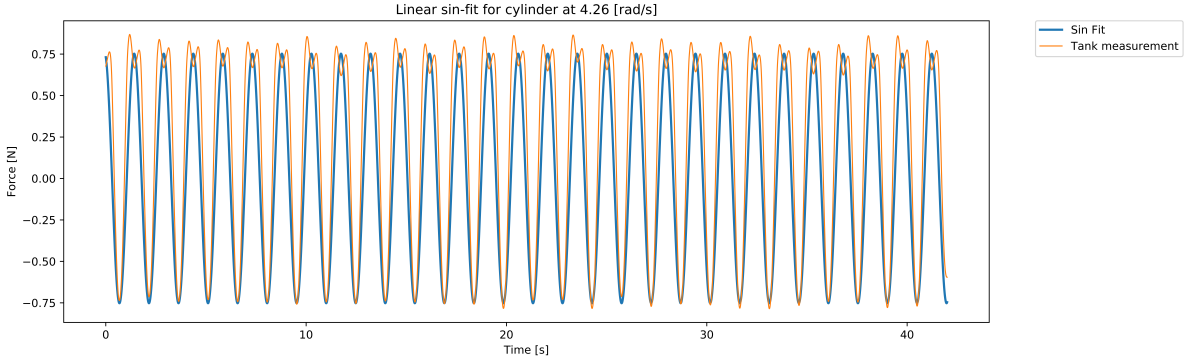

Figure 3.12: Sin-fit on the force signal 4.26 [rad/s]

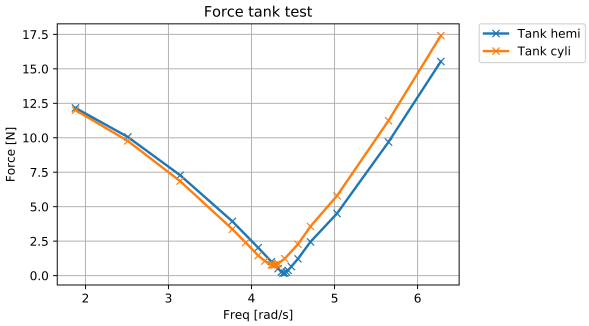

Figure 3.13: Force comparison between Cylinder and Hemisphere

When the amplitude of oscillation decreases, less nonlinear effects are expected. To confirm this expectation, three different amplitudes are measured. In figure 3.14 an example is shown for the time traces at the natural frequency of the cylinder for three amplitudes. Although there is still some nonlinearity present in the measurement at 0.3 [cm], a decrease is clearly visible.

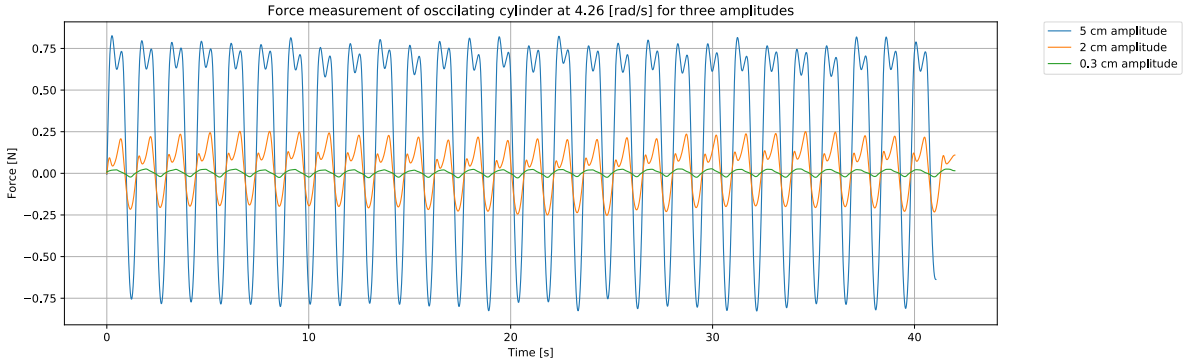

Figure 3.14: Force comparison between different oscillation amplitudes

3.3.2. Added mass and damping

Now the parameters of the sin-fit are known, the added mass and damping coefficients could be obtained by equations 3.1 and 3.2. The phase output of the sin-fit is an important variable for the outcome of the calculations. As is expected, the cylinder has higher values for both added mass and damping due to the shape of the geometry. An observation that is less accurate is the non converging value of the added mass. In theory the added mass becomes a constant with increasing frequency. Unfortunately the oscillator had a limited range so higher frequencies could not be measured. Another observation which is hard to clarify is the negative damping for the hemisphere at the highest frequencies. The reason could lie in the linear approach that is used to find the phase difference between the displacement and force data. In chapter 5 the nonlinear approach is used to obtain more information on this matter.

$$a = \frac{c + \frac{F_a}{z_a}\frac{\cos\varepsilon_{F_z}}{\cos\varepsilon_{z_a}}}{\omega^2} - m \tag{3.1}$$

$$b = \frac{\frac{F_a}{z_a}\frac{\sin\varepsilon_{Fz}}{\sin\varepsilon_{z_a}}}{\omega} \tag{3.2}$$

In the graphs below, in figure 3.15 and 3.16, the obtained added mass and damping coefficients of the two geometries are visualised.

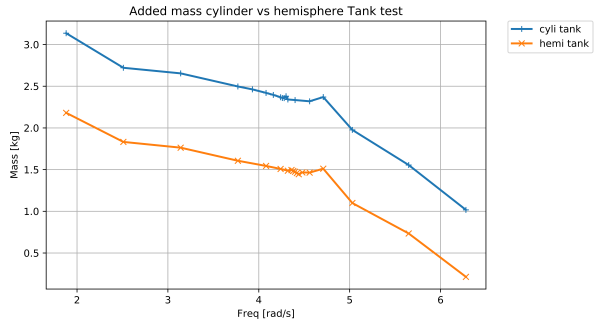

Figure 3.15: Added mass coefficient

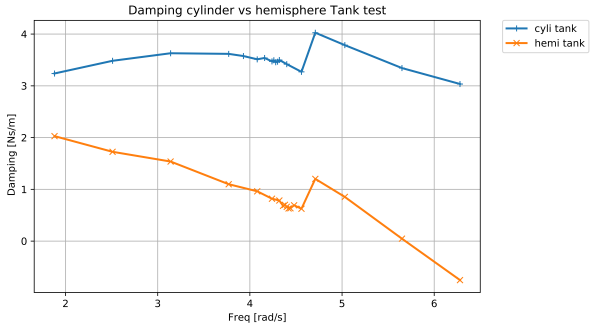

Figure 3.16: Damping coefficient

3.3.3. Free decay

For the free decay-test, the logarithmic decrement is of interest. This shows the steepness of the decrease between the peaks after one period of oscillation. With equation 3.3 the logarithmic decrement can be calculated. In reality, this calculation gives an indication of the value of the decrement. After the calculations, the value is adjusted manually until the curve fitted the decrease of the peaks in the best possible way. As earlier mentioned, the free decay tests are conducted for three initial amplitudes. For each amplitude a slightly different value for the decrement was found and is listed in table 3.5. For the cylinder at an amplitude of 5 [cm], the decrement could not be fitted. In this case, two values are stated; one to match the first two peaks, and one to match the first and last peak. In figures 3.17 and 3.18 the motion measurements are shown and the obtained logarithmic decrements are plotted with the help of equation 3.4. Important to note is the different time scales of the two measurements. Where the cylinder needs under 20 seconds to get back to its static equilibrium, the hemisphere needs at least 60 seconds. During the free-decay tests the geometries oscillate at their natural frequency which are respectively for the cylinder and hemisphere: $\omega_{0_{cyli}}$=4.22 [rad/s] and $\omega_{0_{hemi}}$=4.37 [rad/s].

$$\nu T = \ln\left\{\frac{z(t)}{z(t+T)}\right\} \tag{3.3}$$

$$z = z_a e^{-\nu t} \tag{3.4}$$

Table 3.5: Logarithmic decrements tank test

Logarithmic damping (v)				
	5 [cm]		7.5 [cm]	10 [cm]
Cylinder	0.28	0.11	0.2	0.175
Hemishpere	0.055		0.038	0.049

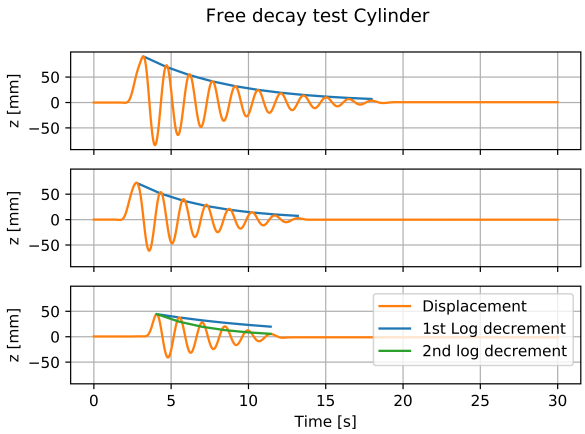

Figure 3.17: Damping of the cylinder at 10, 7.5 and 5 [cm]

Figure 3.18: Damping of the hemisphere at 10, 7.5 and 5 [cm]

3.4. Uncertainties

All experiments are sensitive for uncertainties. Small discrepancies during the measurements could be caused by: human error during construction of the model, roughness of the geometries, friction of the air-bearing, the reflection of the tank walls / beach or post-process methods. In all cases it is tried to keep the uncertainties negligibly small by conducting check runs and by working as accurate as possible. One uncertainty requires extra attention which is the sensitivity of the sin-fit method during post processing.

3.4.1. Sensitivity Analysis

The forced-motion measurements of the cylinder and hemisphere at their natural frequencies, respectively: $\omega_{0cyli} = 4.26$ [rad/s] and $\omega_{0hemi} = 4.40$ [rad/s], are considered during the sensitivity analysis. The influence the value of the cut-off frequency has on the output parameters of the sin-fit, amplitude and oscillation period, are examined by increasing the cut-off frequency four times. The relative change in oscillation frequency compared with the known frequency of the motion is listed in table 3.6, together with the corresponding force amplitude. It is clear to see at which cut-off frequency the sin-fit tool creates irrelevant output. The influence on the force amplitude is max 0.08 [N] for the cylinder and 0.01 [N] for the hemisphere which corresponds to respectively 10% and 6 %.

Table 3.6: Sensitivity analysis sin-fit tool

Sensitivity analysis			
	Cut-Off freq [Hz]	Amplitude [N]	Freq change (ω_0) [%]
Cylinder	1	0.76911	0
	1.5	0.77619	0
	3	0.77888	0
	9	0.67801	-1300
Hemishpere	0.9	0.18094	0
	1.2	0.18165	0
	1.4	0.18062	0
	1.5	0.41668	-200

4

Linear Model

To be able to compare the results of the tank tests, first a linear analytic model is established. For this model, hydrodynamic parameters are needed that are obtained the open source program NEMOH. This is a boundary element methods (BEM) code based on linear potential flow theory [1]. The input can consist of multiple body meshes together with a desired loadcase. From the output of NEMOH, the hydrodynamic coefficients; added mass and damping, in the frequency domain are obtained. The bodies and meshes are generated with the open source program Salome [10].

Highlights chapter 4

- Construction of geometries and mesh files in Salome.
- Load case information on the numerical simulation to resemble the experimental set-up.
- Linear forced motion calculations.
- Hydrodynamic parameter results and contributions in the linear equation of motion.

4.1. Salome

Salome is an open source software framework that provides a CAD modelling tool and is able to generate meshes that can be used in various numerical solvers [10]. In this particular case the software is used to model the two cylinders together with the test tank walls to create an environment that corresponds to the experimental set-up. Only the underwater part of the geometries is modelled and meshed as NEMOH is not able to solve parts above the waterline. In the following subsection the geometries are illustrated.

4.1.1. Geometries

In figure 4.1 and 4.2 the two geometries are illustrated in the Salome model building environment.

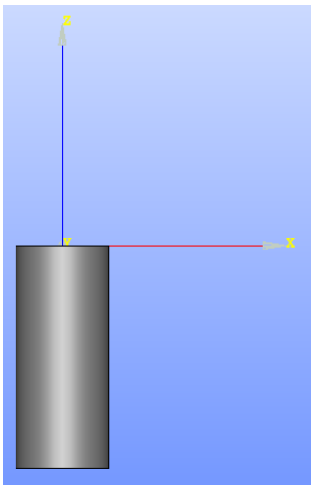

Figure 4.1: Cylinder geometry.

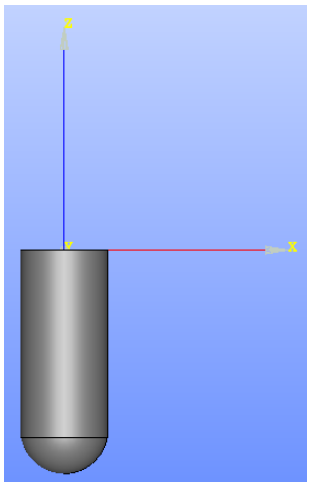

Figure 4.2: Cylinder geometry with hemispheric bottom.

4.1.2. Mesh

In figure 4.3 and 4.4 the two meshes of the geometries are illustrated. The mesh size is set at 0.00985 [cm]. In section 4.4 a mesh convergence study is performed to justify this value.

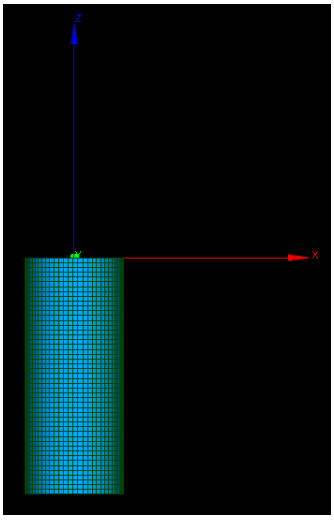

Figure 4.3: Cylinder mesh.

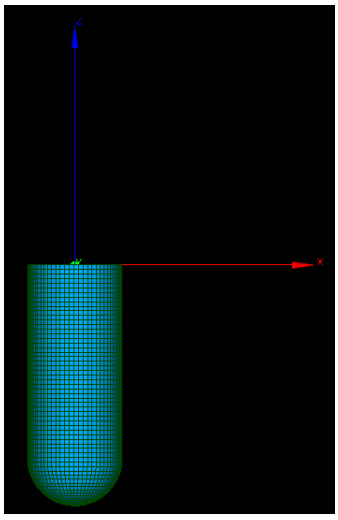

Figure 4.4: Cylinder mesh with hemispheric bottom.

4.1.3. Tank Walls

The full length of the tank walls is meshed and used as input for the solver. In figure 4.5 the walls are visualised in the horizontal plane. Again, only the underwater part is meshed which has a length of 80 [m] and a height of 1.2 [m] which corresponds to the water depth that is used during the forced oscillation tests.

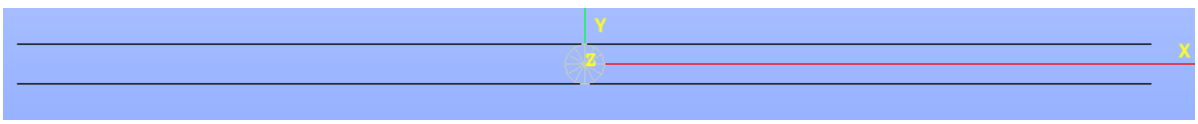

Figure 4.5: Mesh of the tank walls

4.2. NEMOH

NEMOH is one of the few open source BEM solvers on the market and is often used for estimating the hydrodynamic parameters of wave energy converters [16]. The code structure consists of three parts. The preprocessor, where the mesh is prepared and the user inputs for the calculations are read. The solver, calculates the boundary value problems for the potential and the postprocessor writes the hydrodynamic coefficients in a file. In this section the theory behind the solver is explained, an example of the user input is given and the output of the calculations is illustrated.

4.2.1. Theory

NEMOH is a linear BEM code that solves linear boundary value problems (BVP) in the 3-dimensional space. The code is based on potential flow which includes the assumptions that the fluid is inviscid 4.1, the flow is irrotational and incompressible 4.2 and the velocity field can be derived from the flow potential 4.3. Furthermore, the pressure can be obtained using the Bernoulli equation 4.4 [1].

$$\nu = 0 \tag{4.1}$$

$$\begin{cases} \vec{\nabla} \cdot \vec{U} = 0 \\ \vec{\nabla} \times \vec{U} = \overrightarrow{0} \end{cases} \tag{4.2}$$

$$\vec{U} = \vec{\nabla}\Phi \tag{4.3}$$

$$p + \rho g z + \frac{1}{2}(\vec{\nabla}\Phi)^2 + \rho \frac{\partial \Phi}{\partial t} = \text{Cste} \tag{4.4}$$

On the surface of the body, a source distribution problem is created from a flow problem using the method of Green's functions [16]. The BVP's are solved in the frequency domain so to compare it with the tank test results, the hydrodynamic parameters are used in the linear equation of motion including a time vector. In section 4.3.1 this method is explained.

4.2.2. Load cases

Next to the mesh file, another input file is generated to assign the desired calculations NEMOH has to execute. The variables used for this research are: Number of bodies, their degrees of freedom, desired force-components per body and the frequency range and step-size. The amount of bodies is constant for every simulation and consists of two walls and the geometry. Both walls are fixed in all degrees of freedom and the geometry is free to move in the heave direction only. Only the hydrodynamic parameters in the z-direction are of interest in this research. To have comparable results with the tank test, the frequency range is set from 1.8 to 6.5 [rad/s] with steps of 0.025 [rad/s]. In section 4.4, the determination of the frequency stepsize is further elaborated.

4.3. Results

In the following subsections, the obtained results from the linear analytic model are elaborated on and a first analysis is given. First, the method to find the force amplitude and time trace per frequency will be stated to continue with the hydrodynamic parameters that are obtained. In the last subsection, the linear model of the free decay test is explained.

4.3.1. Force

With the added-mass and damping coefficients obtained from NEMOH the force per frequency is calculated with the help of the linear equation of motion 4.5. During the forced motion test, the displacement, velocity and acceleration are imposed and therefore known, see equation 4.6. A time array with the same duration as a test run is created with a time step of 0.1 [s]. The restoring force coefficient, c, is calculated with equation 4.7 and is the same in all test cases. An example of a simulation for the cylinder at 4.26 [rad/s] is given in figure 4.6. In figure 4.7, the forces for all frequencies is given for the cylinder with walls. A small discrepancy is visual at 3.15 [rad/s] which is caused by the value of the added mass and damping coefficient. In next subsection, this will be elaborated.

$$(m + a)\ddot{z} + b\dot{z} + cz = F_z(t) \tag{4.5}$$

$$z = z_a \cos(\omega t + \varepsilon_{z\zeta})$$
$$\dot{z} = -z_a \omega \sin(\omega t + \varepsilon_{z\zeta}) \tag{4.6}$$
$$\ddot{z} = -z_a \omega^2 \cos(\omega t + \varepsilon_{z\zeta})$$

$$c = \pi \rho g r^2 \tag{4.7}$$

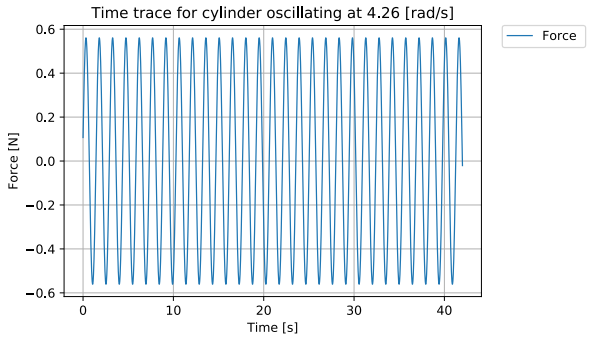

Figure 4.6: Simulation example for Cylinder at 4.26 [rad/s]

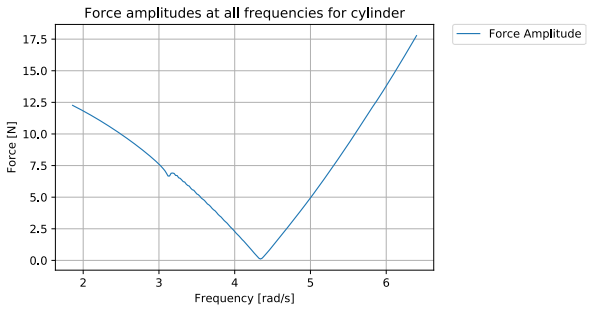

Figure 4.7: Force amplitude at all frequencies for Cylinder with tank walls

4.3.2. Added mass and damping

The added mass [kg] and damping [Ns/m] coefficients are retrieved from the output file using a generic python script which is able to locate the coefficients according to the input file. The graphs in figures 4.8 and 4.9 present the hydrodynamic coefficients related to the frequency. Remarkable is the almost exact same results for the damping coefficients for both the geometries. Because NEMOH only calculates the potential damping coefficient no friction, vortices and separation phenomena are taken into account. As the shape of the waterline area is the same it seems logical that the two geometries have the same damping coefficient. A clear difference between the simulation with and without the tank wall is seen. This difference can be explained by the fact that reflected waves from the side walls influence the motion of the geometries and therefore the coefficients. With Bob You's approximation the wave lengths and velocities are calculated at all frequencies for a water depth of 1.2 [m][19]. At 3.15 [rad/s] the disturbance is highest which is the point where the wavelength of the radiated wave is exactly two times the width between the tank walls. In section 5.1.1 of next chapter, the accuracy of the linear approach towards estimating the hydrodynamic parameters is assessed by comparing the numerical and experimental obtained hydrodynamic parameters.

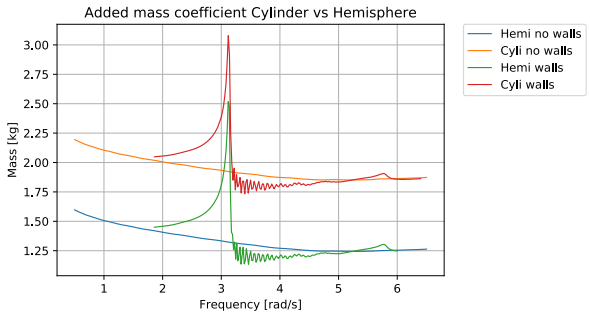

Figure 4.8: Added mass coefficient for all frequencies

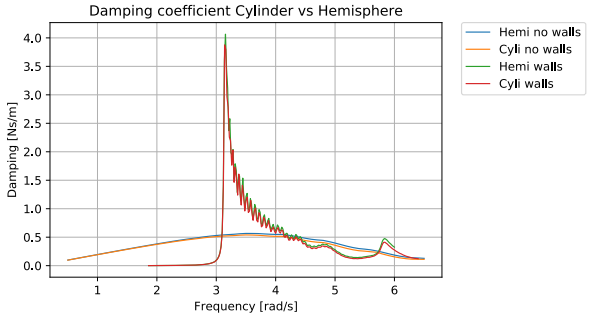

Figure 4.9: Damping coefficient for all frequencies

Now the values of the linear hydrodynamic coefficients are known, the influence they have on the results of the analytic model is studied. In figure 4.10 the absolute force contribution of the added mass and damping term in the motion equation are plotted. Figure 4.11 illustrates the three different terms in the motion equation. Important to know is the 180 degree phase difference between the restoring stiffness and the inertia term which means they cancel out at the natural frequency. So in theory, although the damping term is

small, at the natural frequency it has a 100% contribution in the total force output. The graph emphasizes the location of dominant terms in the motion equation as earlier stated in section 2.2.

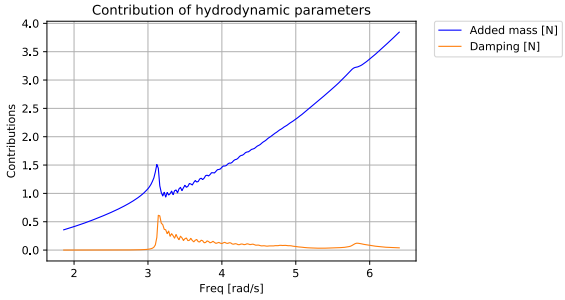

Figure 4.10: Added mass and damping contribution

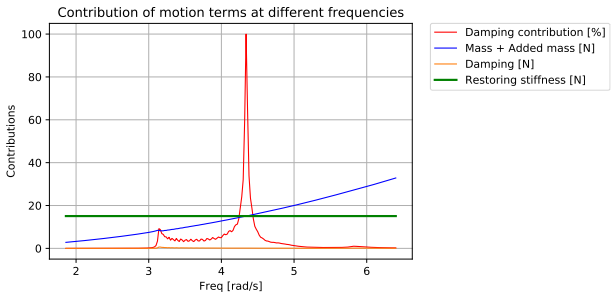

Figure 4.11: Contribution of motion terms

4.3.3. Free decay

For the analytic model of the free decay test, the added mass and damping coefficients at the natural frequencies of the two geometries are used to calculate, with equation 4.8, the damping coefficient of the logarithmic decrement. The the time trace of the free decay test is established with equation 4.9. In figures 4.12 and 4.13 the results are illustrated. The values of the logarithmic damping coefficients are listed in table 4.2.

$$2v = \frac{b}{m+a} \tag{4.8}$$

$$z = z_a e^{-vt}\left(\cos\omega_0 t + \frac{v}{\omega_0}\sin\omega_0 t\right) \tag{4.9}$$

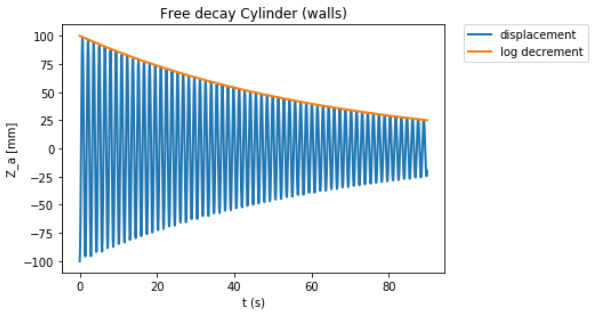

Figure 4.12: Simulation of free decay test cylinder with tank walls

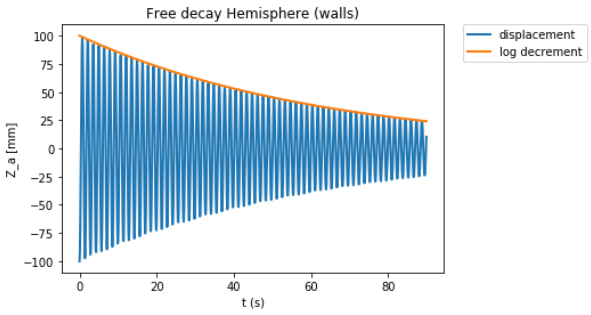

Figure 4.13: Simulation of free decay test hemisphere with tank walls

Table 4.1: Logarithmic decrement coefficients

Logarithmic decrement (v)		
	Walls	No walls
Cylinder	0.0154	0.0175
Hemishpere	0.0158	0.0180

4.4. Sensitivity analysis

To ensure the acquired data obtained from NEMOH is correct, the influence of the frequency step-size and the mesh-size of the geometries are studied. In figures 4.14 to 4.19 first, the frequency step-size is considered continued by the mesh size influence considering the case with and without tank walls. In cases where the

tank walls are present, the graphs are zoomed at 3.15 [rad/s] as this was frequency where the influence of the step-size and mesh-size was largest. The medium size mesh corresponds to a mesh size of 0.00985 [cm] while the rough mesh has a size of 0.0197 [cm]. The values used in this chapter are $df = 0.025[rad/s]$ and $mesh - size = 0.0197[cm]$.

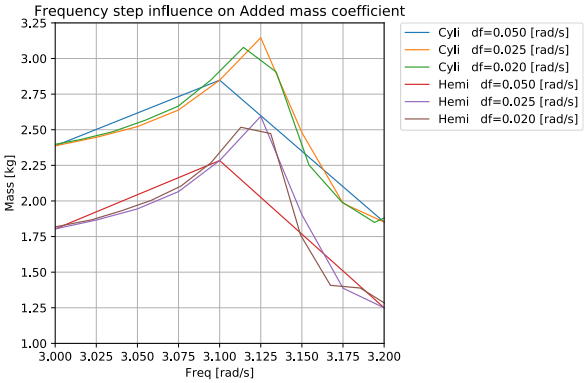

Figure 4.14: Frequency step-size influence on added mass coefficient

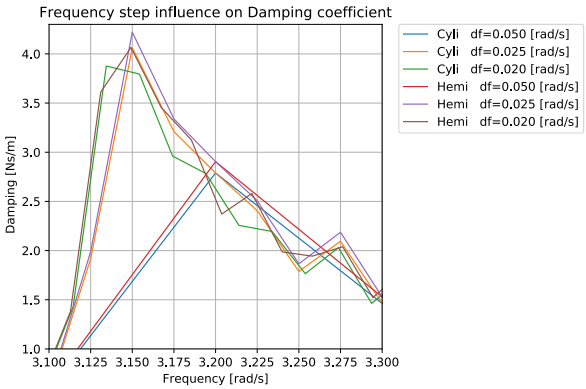

Figure 4.15: Frequency step-size influence on damping coefficient

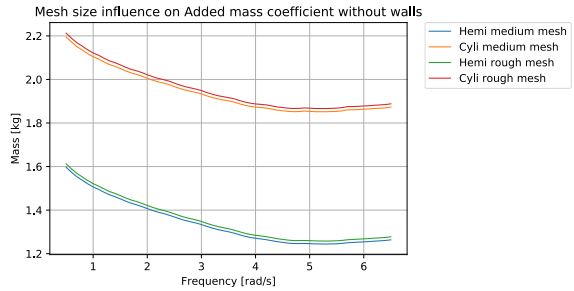

Figure 4.16: Added mass coefficient for all frequencies

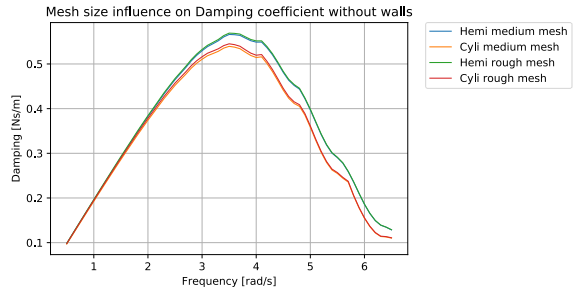

Figure 4.17: Damping coefficient for all frequencies

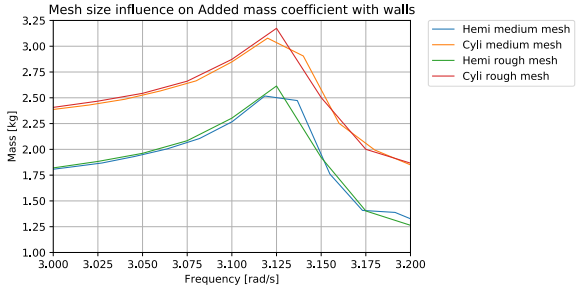

Figure 4.18: Added mass coefficient for all frequencies

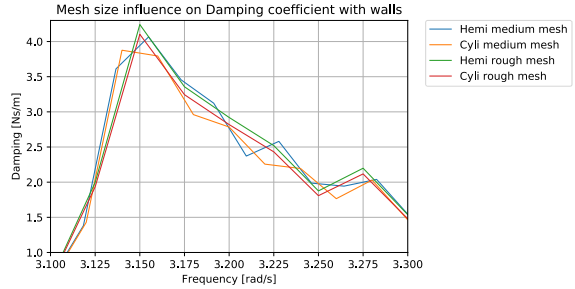

Figure 4.19: Damping coefficient for all frequencies

5

Nonlinear Analysis

With the information obtained from the experiment and the linear anlytic model, the behaviour of the nonlinear viscous damping can be captured and the hypothesis of this thesis can be investigated. In this chapter the nonlinear behaviour is analysed and approached by a quadratic damping term in the motion equation. The goal is to establish a relation of the vertical drag coefficient over the frequency of oscillation. The state of the art in determining the drag coefficient is applied on the data and compared with the performance of a new nonlinear analytic model. First, the combined results of the previous chapters are analysed to have a clear view of the viscous drag force behaviour.

Highlights chapter 5

- Assessment of the experimental and linear numerical method for obtaining hydrodynamic parameters.
- Description of the vertical viscous drag force behaviour over the frequency domain.
- Comparison between three analytic models describing the viscous drag force.
- Established relationship of the vertical drag coefficient over the frequency of oscillation.

5.1. Analysis of obtained results

In this section, the results of the tank test and linear analytic model are combined to quantify the viscous force influences. First the added mass and damping is discussed as these results have influence on the force results which are discussed in the second subsection.

5.1.1. Added mass and damping coefficients

In figures 5.1 and 5.2 the obtained added mass and damping coefficients obtained from NEMOH and the tank tests are plotted in the same graph.

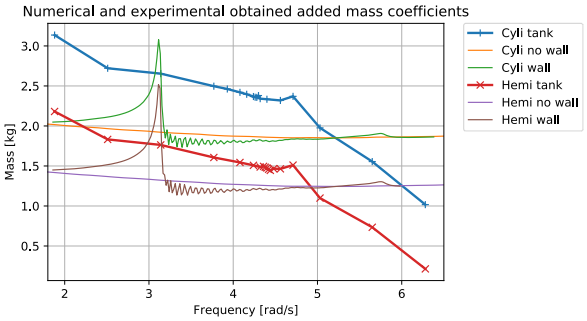

Figure 5.1: Added mass tank test and simulations

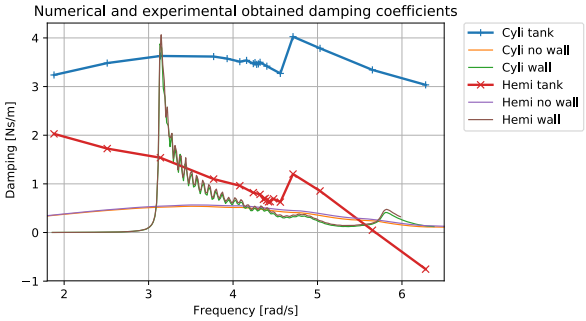

Figure 5.2: Damping tank test and simulations

A clear difference between the numerical results with and without the tank wall is seen. This difference can be explained by the fact that reflected waves from the side walls influence the motion of the geometries and therefore the coefficients. With Bob You's approximation the wave lengths and velocities are calculated at all frequencies for a water depth of 1.2 [m][19]. At 3.15 [rad/s] the disturbance is highest which is the point where the wavelength of the radiated wave is exactly two times the width between the tank walls. This irregular frequency creates a mathematical problem in the boundary integral equation in the numerical solver. This is not a physical problem and therefore this disturbance is not seen in the results of the experiment. It can be stated that the linear approximation with tank walls is not able to correctly estimate the value of the coefficients.

As expected, the value of the added mass coefficient is larger for the cylinder due to the shape of the geometry. A same trend can be seen in the numerically obtained values from NEMOH where no wall is present, except, after the natural frequency this trend changes. Here, it is expected that the values converge as they do for the solver results. Another observation is the underestimated added mass values before and at the natural frequencies of the solver results. This difference in mass is exactly the mass that causes the shift in natural frequency of the linear analytic model compared with that of the tank test. As this study focusses only on the nonlinear viscous damping, this difference in mass is added in the linear model so the natural frequencies of both methods correspond with each other. The value of this mass difference is for the cylinder and hemisphere respectively $0.60[kg]$ and $0.34[kg]$

The linear damping coefficient is dependent on the waterline area of the geometry and therefore the same for both the cylinder and hemisphere. When comparing the experimental results, a significant difference can be noticed. This is expected as more viscous effects are present for the cylinder and therefore a higher damping coefficient is logical.

In a study of F. Ferri et al. [3], differences between coefficients obtained from a BEM solver and experimental tests were also present. This study explained the error by the small contribution of the coefficients in the total system of motion. In section 4.3.2 of previous chapter the contributions of the coefficients are illustrated. With this information, it can be stated that the accuracy of determining the added mass and drag coefficients from this experiment decreases rapidly when moving away from the natural frequency of the system.

The results show that the value of the hydrodynamic parameters is hard to estimate with a linear solver due to the fact no viscous damping is present. Furthermore, determining the parameters from the experiment is error sensitive when other terms in the motion equation dominate.

5.1.2. Force

The force deviations between the linear analytic and the experimental results are largest around the natural frequencies of the geometries. In figures 5.3 and 5.4 the force amplitudes are plotted for the cylinder and hemisphere. The force amplitudes of the linear model are only 13% and 29% of the measured force amplitude for respectively the cylinder and hemisphere oscillating at their natural frequency.

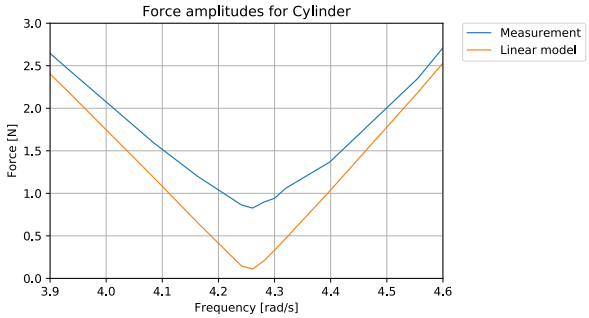

Figure 5.3: Viscous drag force influence for cylinder

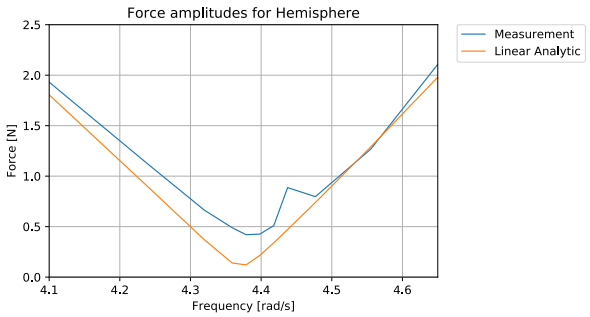

Figure 5.4: Viscous drag force influence for hemisphere

In the force time-traces of the measurements near the natural frequencies, the effect of the viscous damping is clearly visual. In figures 5.5 and 5.6 the linear analytic result and tank measurement for the cylinder and hemisphere are plotted in the same graph. It can be noticed that in the force time-trace of the measurements no symmetry is present in the $F = 0$ axis. This means, the viscous forces behave different when moving down than moving up.

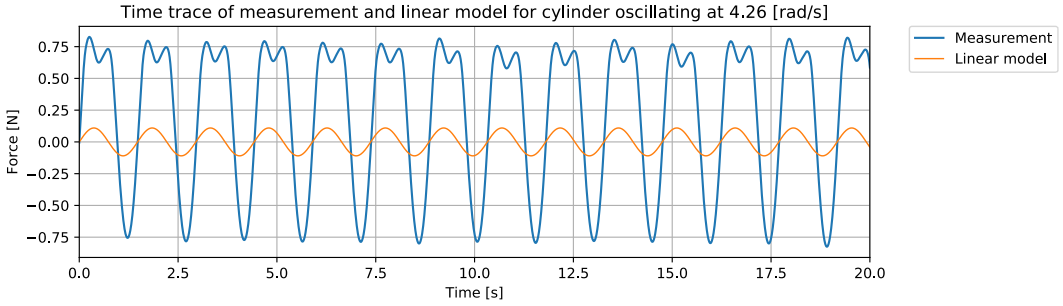

Figure 5.5: Tank measurement and linear analytic force time trace of cylinder oscillating at its natural frequency

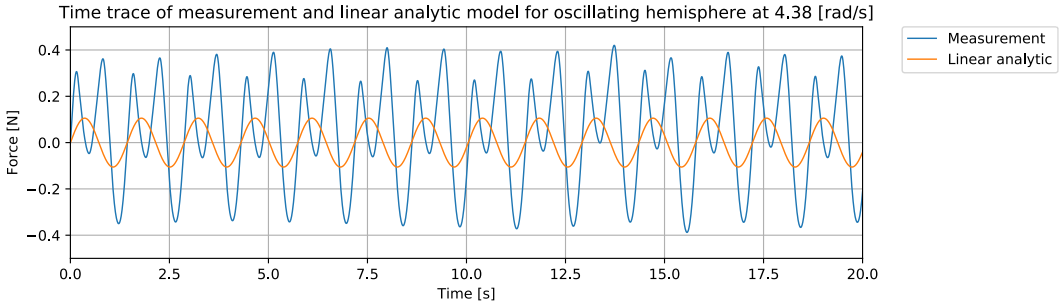

Figure 5.6: Tank measurement and linear analytic force time trace of hemisphere oscillating at its natural frequency

The significance of the viscous drag force is well presented by the difference in the damping time between the linear analytic and experimental approach for the free decay test. In figure 5.7 the damping time for all cases is illustrated.

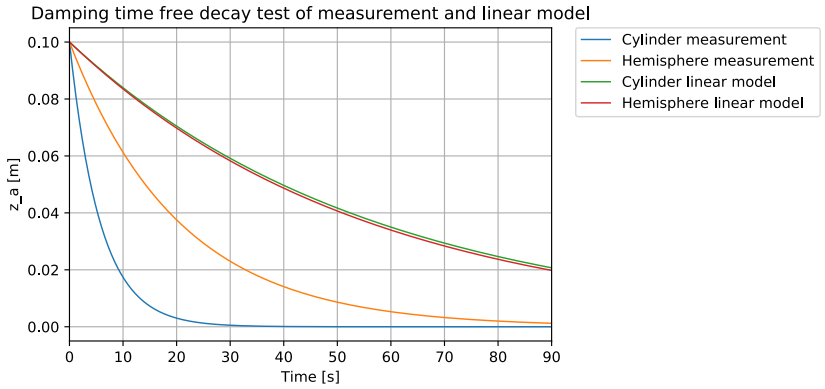

Figure 5.7: Logarithmic decrements for all cases (nonlinear part shaded)

5.2. Determination of the drag coefficient

As earlier stated, experiments have shown that the drag force is dependent upon the flow velocity squared [7]. Different methods are used in the past to determine the drag coefficients. In this section the damping term in the motion equation is isolated containing the linear radiation damping and the nonlinear viscous damping (equation (5.2)). As formula (2.7) calculates the drag force per unit length, the formula is multiplied by the diameter of the cylinder to obtain the total drag force over the width of the cylinder. Four methods are presented for obtaining the drag coefficient starting with a widely accepted design method based on empirical obtained data from the past. The three other methods are based on a least square fit applied on the experimental data obtained in this research. As the experiments were conducted in still water, the flow velocity is equal to the vertical velocity of the oscillating cylinder: $\dot{z} = z_a \cdot \omega cos(\omega t + \epsilon)$.

$$F_D(t) = \frac{1}{2}\rho \underline{C_D} D \dot{z}|\dot{z}| \tag{5.1}$$

$$\begin{aligned} F_z(t) &= F_{\text{inertia}} + F_{\text{damping}} + F_{\text{stiffness}} \\ F_{\text{damping}}(t) &= \underline{b} \cdot \dot{z} + \tfrac{1}{2}\rho \underline{C_D} D \cdot \dot{z}|\dot{z}| \end{aligned} \tag{5.2}$$

5.2.1. Keulegan Carpenter

The KC-number, calculated with equation (5.3), is for all frequencies 1.6. This because the oscillation frequency is cancelled in the equation. If figure 2.10 is recalled, the x-axis starts at KC=2.5. Little information is found on drag coefficient for low KC number flows as in this area the viscous drag is often neglected.

In a design method proposed by classification bureau Det Norske Veritas, also the drag coefficients are defined for low KC-numbers, see figure 5.8[7]. If this figure is followed, considering a smooth cylinder, a drag coefficient of 1 should be used in the estimation of the drag force component. For this method, the total damping force is calculated using the linear damping coefficient obtained from the numerical solver in combination with a drag coefficient of 1. In the results, this method is referred to as "KC".

$$KC = \frac{\dot{z}_{max} \cdot T_\omega}{D} = \frac{z_a \cdot \omega \cdot \frac{2\pi}{\omega}}{D} = \frac{z_a \cdot 2\pi}{D} = 1.6 \tag{5.3}$$

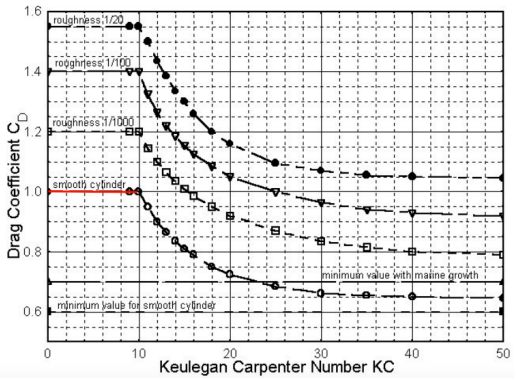

Figure 5.8: KC-number related to the drag coefficient for a cylinder [7]

5.2.2. Least squares fit 1

For this method, the scipy.optimize.curve-fit function is used in Python. This function tries to minimise the sum of the least squares error between the input data and a given fit function by optimizing the variables in the fit function. The measured force signal of the experiment is used as input data and the fit function consist the motion equation including the damping term with the, to be optimized, variables see equation 5.4.

$$R\left(F_{\text{damping}}\right) = \int_0^T \left\{F(t)_{\text{measured}} - F_z\left(t, F_{\text{damping}}\right)\right\}^2 dt \tag{5.4}$$

The variables to optimize in the damping force contain the linear damping coefficient, b, the drag coefficient, C_D, and the phase of the velocity component, ϵ. The total fit function is showed in equation 5.5.

$$\begin{gathered} F_z(t, F_{\text{damping}}) = F_{\text{inertia}}(t) + F_{\text{damping}}(t, b, C_D, \epsilon) + F_{\text{stiffness}}(t) \\ F_{\text{damping}}(t, b, C_D, \epsilon) = \underline{b} \cdot z_a\omega \cdot cos(\omega t + \underline{\epsilon}) + \tfrac{1}{2}\rho \underline{C_D} D \cdot (z_a\omega \cdot cos(\omega t + \underline{\epsilon})) \cdot |z_a\omega \cdot cos(\omega t + \underline{\epsilon})| \end{gathered} \tag{5.5}$$

In this function the absolute velocity is used to correct for the sign as the velocity is oscillating. Unfortunately the results of the method where not satisfying so a closer look into the characteristics of the measured force signal is taken in the next subsection. In the results this method is referred to as "Fit 1".

5.2.3. Least squares fit 2

A Fast Fourier Transform (FFT) is applied on the measured force data to see the dominating frequencies that are present in the signal. In figures 5.9 and 5.10 the plots of the transforms at the natural frequencies of the geometries are illustrated. The first peak in the graphs show the linear first order effects that correspond to the driving frequency of the motion. The second peak is at twice the driving frequency and shows the influence of the second order nonlinear behaviour in the measured signal that is expected to correspond to the viscous drag force. As can be noticed, the nonlinear effects have a, relatively, larger contribution for the hemispheric geometry. The influence of the second order nonlinear effects vanishes when the driving frequency moves away from the natural frequencies of the geometries.

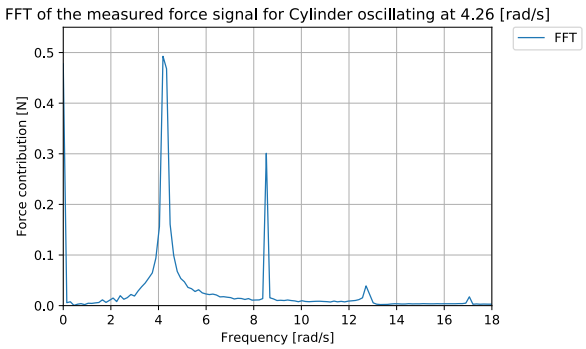

Figure 5.9: Fourier analysis of force signal cylinder

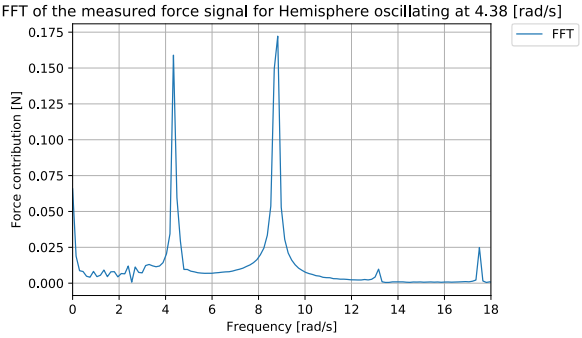

Figure 5.10: Fourier analysis of force signal frequency

With this information the quadratic velocity term is further analysed to find a relation where twice the driving frequency is present. To establish this, the absolute velocity term in equation 5.5 is replaced by the normal velocity. Use is made of the trigonometric similarities to link the velocity squared with the period-doubling bifurcation of the system. The following relation can be derived:

$$\dot{z} \cdot \dot{z} = (z_a\omega \cdot cos(\omega t + \epsilon))^2 = \frac{1}{2} {z_a}^2\omega^2 + \frac{1}{2} {z_a}^2\omega^2 \cdot cos(2\omega t + 2\epsilon) \tag{5.6}$$

In this relation, the second driving frequency becomes visual. Because no absolute velocity is present, the time trace will stay positive. In figure 5.11 an example of the time traces of both the quadratic velocities terms is illustrated. To correct for the positive sign of the quadratic term, an extra variable is added to the fit function in the form of an offset. Except for the offset, the same variables are used as in the previous subsection. The new fit function is show in equation 5.7:

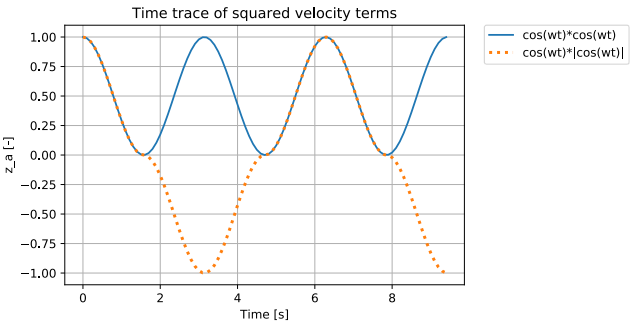

Figure 5.11: Time traces of the quadratic velocity terms

$$F_z(t, F_{\text{damping}}) = F_{\text{inertia}}(t) + F_{\text{damping}}(t, offset, b, C_D, \epsilon) + F_{\text{stiffness}}(t)$$

$$F_{\text{damping}}(t, offset, b, C_D, \epsilon) = \underline{offset} + \underline{b} \cdot z_a \omega \cdot cos(\omega t + \underline{\epsilon}) + \tfrac{1}{2}\rho \underline{C_D} D \cdot (\tfrac{1}{2} {z_a}^2 \omega^2 + \tfrac{1}{2} {z_a}^2 \omega^2 \cdot cos(2\omega t + 2\underline{\epsilon})) \tag{5.7}$$

The results are more satisfying and will be discussed in the next section. This method will be referred to as "Fit 2"

Least square fit 2a

The interest has grown to see how the results of fit 2 would differ if the added mass is added to the set of variables instead of using the numerical obtained linear added mass values. In equations 5.8 and 5.9 the new shape of the fit function is stated. The used damping function is the same as in equation 5.9. This method will be referred to as "Fit 2a"

$$F_z(t, F_{\text{inertia}}, F_{\text{damping}}) = F_{\text{inertia}}(t, a) + F_{\text{damping}}(t, \text{offset}, b, C_D, \epsilon) + F_{\text{stiffness}}(t) \tag{5.8}$$

$$F_{\text{inertia}}(t, a) = (m + \underline{a}) \cdot (-z_a \omega^2 \sin(\omega t)) \tag{5.9}$$

5.3. Results nonlinear analysis

In this section, the results obtained from the different methods are discussed. First, the force amplitudes and time traces are presented and the goodness-of-fit is calculated to define a measure of performance of the used methods. Secondly, the values of the coefficients, including the drag coefficient is presented to find the answer to the main question of this research. Because the results of fit 2 and fit 2a are similar, only the goodness-of-fit values and coefficients of fit 2a are discussed to maintain a clear view of the results.

5.3.1. Force results

In figures 5.12 and 5.13 the force amplitudes obtained from the experiment and the different methods is visualised around the natural frequencies. In case of the cylinder, all the methods show an improvement towards estimating the experimental values. In case of the hemisphere, "Fit 1" is underestimating the drag forces and "Fit 2" has some discrepancies around the natural frequency. "KC" does correctly estimate the force amplitude around the natural frequency. The results seem quite favourable for the "KC" method, especially in case of the hemisphere. But when the time trace is investigated this assumption changes.

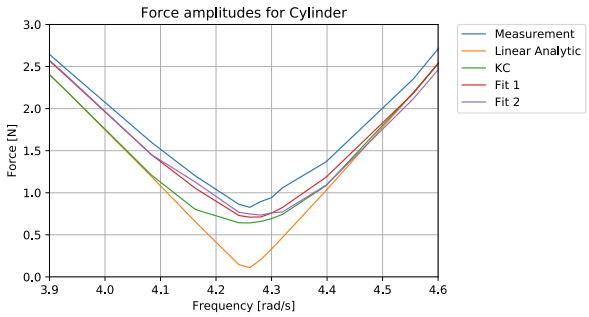

Figure 5.12: Fit result cylinder

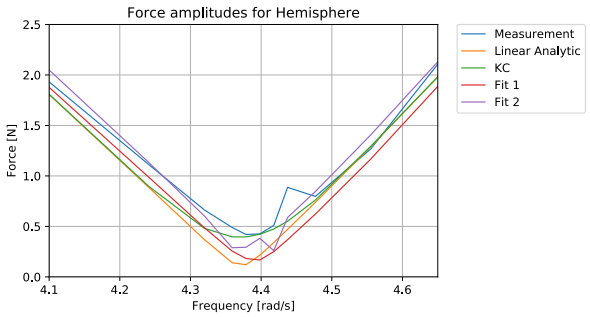

Figure 5.13: Fit result hemisphere

In figure 5.14 and 5.15 the time traces of the different methods are compared with the measurement results. In these figures it is clear to see that the conventional method, "KC" and the fit method including the absolute velocity term do not follow the time trace of the measurement. In appendix A, the time traces at all the frequencies are given.

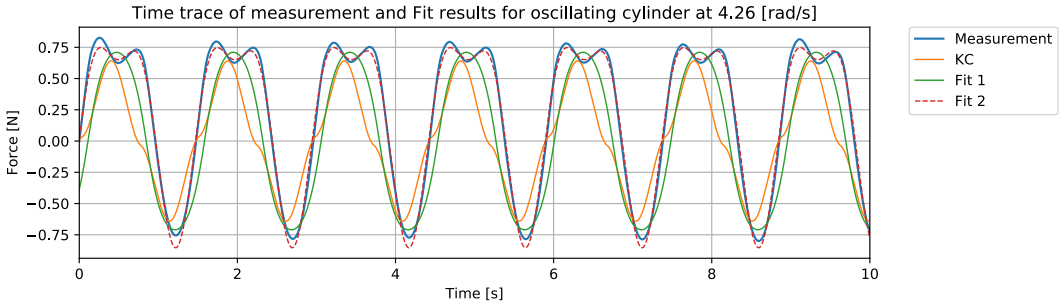

Figure 5.14: Goodness of fit of different methods on the measurement of the cylinder oscillating at the natural frequency

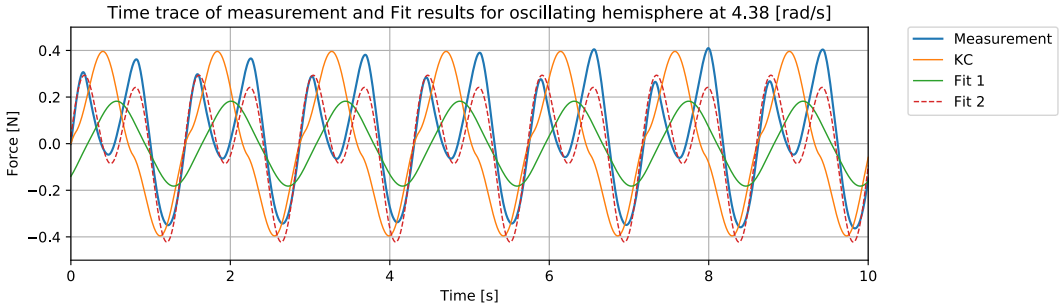

Figure 5.15: Goodness of fit of different methods on the measurement of the hemisphere oscillating at the natural frequency

To measure the goodness of the fit (GoF) , equation 5.10 is used. This equation evaluates the different methods by taking the square root of the sum of the least squares error and divide it by the amplitude of the measured force at each oscillating frequency. In figure 5.16, the dimensionless values are given.

$$\text{GoF} = \frac{\sqrt{\sum_{t=0}^{30} (F_{\text{measured}} - F_{\text{calculated}}))^2}}{F_{a_{\text{measured}}}} \tag{5.10}$$

Cylinder

ω [rad/s]	KC	Fit 1	Fit 2	Fit 2a
1,88	1	1	1	1
2,51	4	2	1	1
3,14	10	6	2	1
3,77	24	14	3	2
3,93	31	18	3	3
4,08	37	24	6	5
4,16	42	30	22	7
4,24	87	58	14	9
4,26	77	61	9	9
4,28	59	50	12	8
4,30	52	44	15	7
4,32	42	37	18	35
4,40	36	31	20	5
4,56	35	26	8	4
4,71	25	19	5	3
5,03	23	13	6	1
5,65	20	7	3	1
6,28	24	5	1	1

Hemisphere

ω [rad/s]	KC	Fit 1	Fit 2	Fit 2a
1,88	2	1	1	1
2,51	3	2	1	1
3,14	7	5	1	1
3,77	19	12	1	1
4,08	38	25	4	2
4,24	63	40	12	6
4,32	78	54	21	8
4,36	114	66	55	10
4,38	110	76	28	12
4,40	101	75	17	11
4,42	178	64	46	10
4,44	55	41	6	6
4,48	78	56	9	7
4,56	66	44	7	6
4,71	30	22	4	4
5,03	29	15	8	1
5,65	21	7	3	1
6,28	26	4	1	0

Figure 5.16: Goodness of fit values

The values emphasize the improvements of the second fit function compared to the method using KC and Fit 1. When the added mass is included as a variable, a slight improvement is noticed. In next subsection the obtained coefficients of fit method 2 and 2a are discussed.

5.3.2. Coefficients

In figures 5.17 and 5.18 the hydrodynamic parameter values obtained from the experiment, numerical simulation and best performing fit methods are illustrated. Although "Fit 2a" has the best performance, the hydrodynamic parameters are highly fluctuating. The large amount of variables in the fit function causes this behaviour. When the added mass is not included ("Fit 2"), the fluctuations decrease and the damping coefficients only fluctuate near the natural frequencies. The damping coefficients for higher oscillating frequencies overestimate the experimental and numerical results. This could be caused by the small contribution of the damping term in the motion equation for higher oscillating frequencies, which will increase the fit uncertainty.

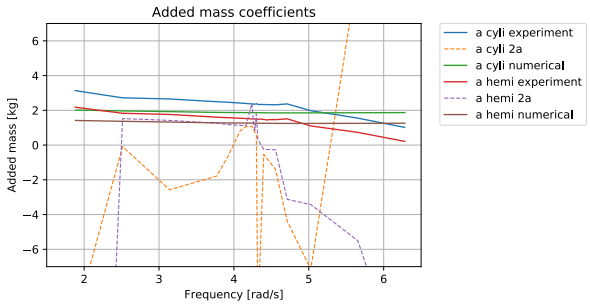

Figure 5.17: Added mass coefficients values obtained from experiment, numerical and "Fit 2a"

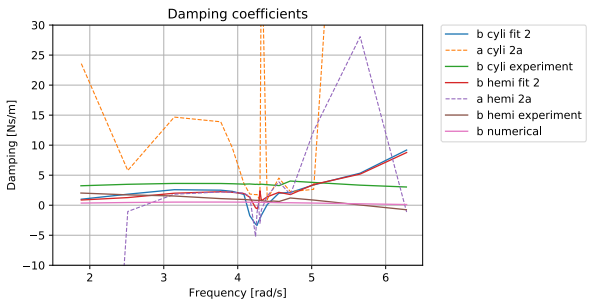

Figure 5.18: Damping coefficients obtained from experiment, numerical and "Fit 2" and "Fit 2a"

In figure 5.19, the obtained drag coefficients from "Fit 2", "Fit 2a" and the KC-method are illustrated. Again the values of the "Fit 2a" method fluctuate, especially near the natural frequencies. What is clear to see is the influence of the oscillation frequency on the value of the drag coefficient. So unlike the assumption of the KC-method, even for small KC values, no constant drag coefficient should be used for estimating the viscous drag force.

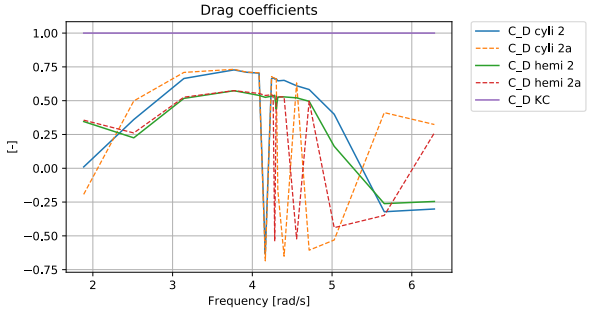

Figure 5.19: Drag coefficients obtained from "Fit 2", "Fit 2a" and "KC" method

5.4. Concluding remarks

In the nonlinear analysis a better understanding is established of the behaviour of the viscous drag. The measured signal can be best described by a function without an absolute velocity term. A probable cause is the non-symmetric time trace of the force signal in the F=0 axis. For this reason, the fit of the conventional drag force formulation, "Fit 1", is able to correctly estimate the force amplitude but does not cover the force time-trace. If a constant drag coefficient is used, the "KC" method, the force amplitude around the natural frequency is well estimated but will be overestimated when the viscous drag is of less importance. This chapter shows that even for low KC-number values, viscous drag is still of importance when looking at oscillating cylinders. Furthermore, the frequency of oscillation has a influence on the drag coefficient and is therefore important to consider when the response of a oscillating buoy is estimated.

6

Conclusions

The vertical viscous drag force acting on a heaving cylinder with flat and hemispheric bases is investigated by means of an experiment and a linear analytic model. The behaviour of the viscous damping is captured and a linear and nonlinear analytic model is created that describes the measured force signal at different frequencies. From the results, the following conclusions are drawn:

Experiment

- When the frequency of oscillation is close to the natural frequency of the geometries viscous damping has a significant contribution in the motion of a WEC.
- The added mass and damping coefficients have a small absolute contribution in the motion equation. Therefore, only around the natural frequencies the damping term becomes visual. For this reason, the hydrodynamic parameters obtained further away from the natural frequencies are uncertain.

Linear model

- Due to the width between the tank walls an irregular frequency occurred at 3.15 [rad/s]. Therefore, the numerical results of the hydrodynamic parameters where the tank walls are present are inaccurate.
- The numerical results without tank walls underestimate the values of the hydrodynamic parameters when compared with the results obtained from the experiment as no viscosity is considered in the numerical method.
- The force amplitudes of the linear model are only 13% and 29% of the measured force amplitude for respectively the cylinder and hemisphere oscillating at their natural frequency.

Nonlinear analysis

- Non-symmetric period doubling characteristics occur in the force measurements near the natural frequency of oscillation.
- Although the flow is oscillating, this characteristic can be captured accurately with a non-absolute velocity squared term in the conventional drag force formulation: $F_D = \frac{1}{2}\rho C_D D|\dot{z}|\dot{z} \rightarrow F_D = \frac{1}{2}\rho C_D D\dot{z}^2$.
- This formulation performs 10 to 20 times better if compared with methods using a constant drag coefficient or using the convention drag force formulation with absolute velocity term.
- Even for small KC-number values, viscous drag influence the damping for an oscillating body. The established relations relating the KC-number with the drag coefficient do not estimate the drag force accurately.
- The drag coefficients varies over the frequency of oscillation.

Can a frequency dependent drag coefficient improve the accuracy in estimating the damping response of a STC hybrid wind-wave energy converter?

The answer is: **Yes** it can. This research provides a new insight in the way the drag coefficient is treated. The results show the importance of the frequency when the motion response of floating, semi-submerged, bodies is considered. Future research is needed to translate the results into an applicable method which is able to estimate the viscous drag analytically.

7

Recommendations

This study demonstrated a first step in showing the importance of the frequency of oscillation in determining the viscous drag forces. To translate the results towards the reality future research is required. In this chapter, recommendations are provided for future research and possible improvements are given for the methods used during this thesis.

- Improve accuracy: The oscillator used in the experiments showed high frequency mechanical disturbances. By increasing the size of the model the force amplitude will increase so the relative influence of this disturbance decreases. Another option is to perform time-consuming CFD simulations to have comparable material to validate the accuracy of the results.
- Perform experiments focussing on the added mass and linear damping only to decrease the amount of unknown variables in the fit function. This will increase the performance of the fit function used in this research.
- Translate the results from the frequency domain to a time domain so the nonlinear viscous effects can be used to describe the free decay damping time.
- Irregular wave tests: In reality the wave energy converter will be excited by irregular waves. Irregular wave tests can be used to see if the obtained results per wave frequency can be adopted to estimate the response of the wave energy converter in irregular waves.
- Find the drag coefficients at full scale: To conclude the recommendations, a full scale CFD simulation can give a good insight in the loads and may predict them with more detail. In this way the response can be calculated and the PTO-damping of the wave energy converter can be optimized.

A

Time traces

Time traces at all frequencies

In this appendix, all the time traces of the force measurements and methods are listed per frequency. First the cylinder results are shown to continue with the hemisphere results.

Cylinder

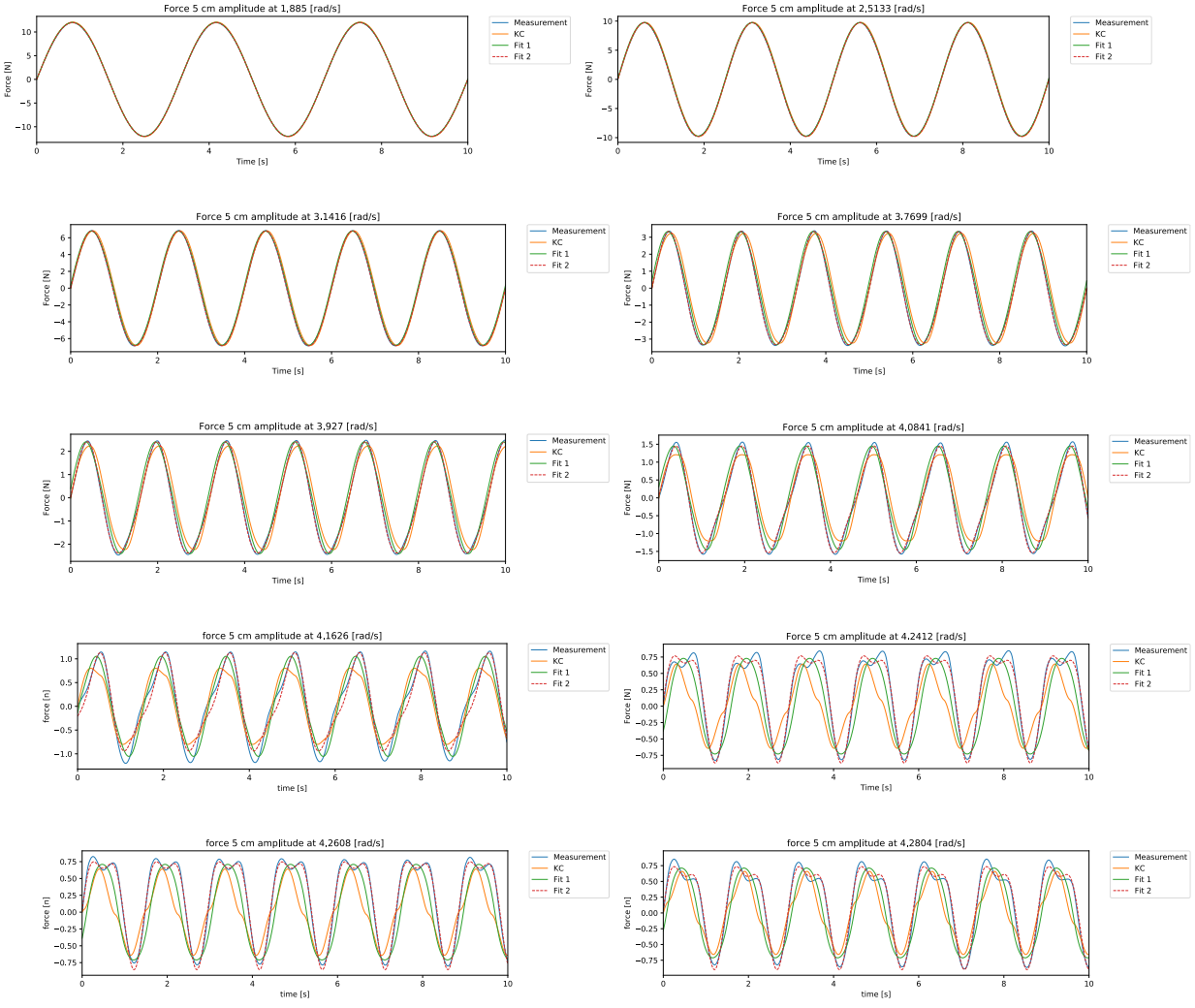

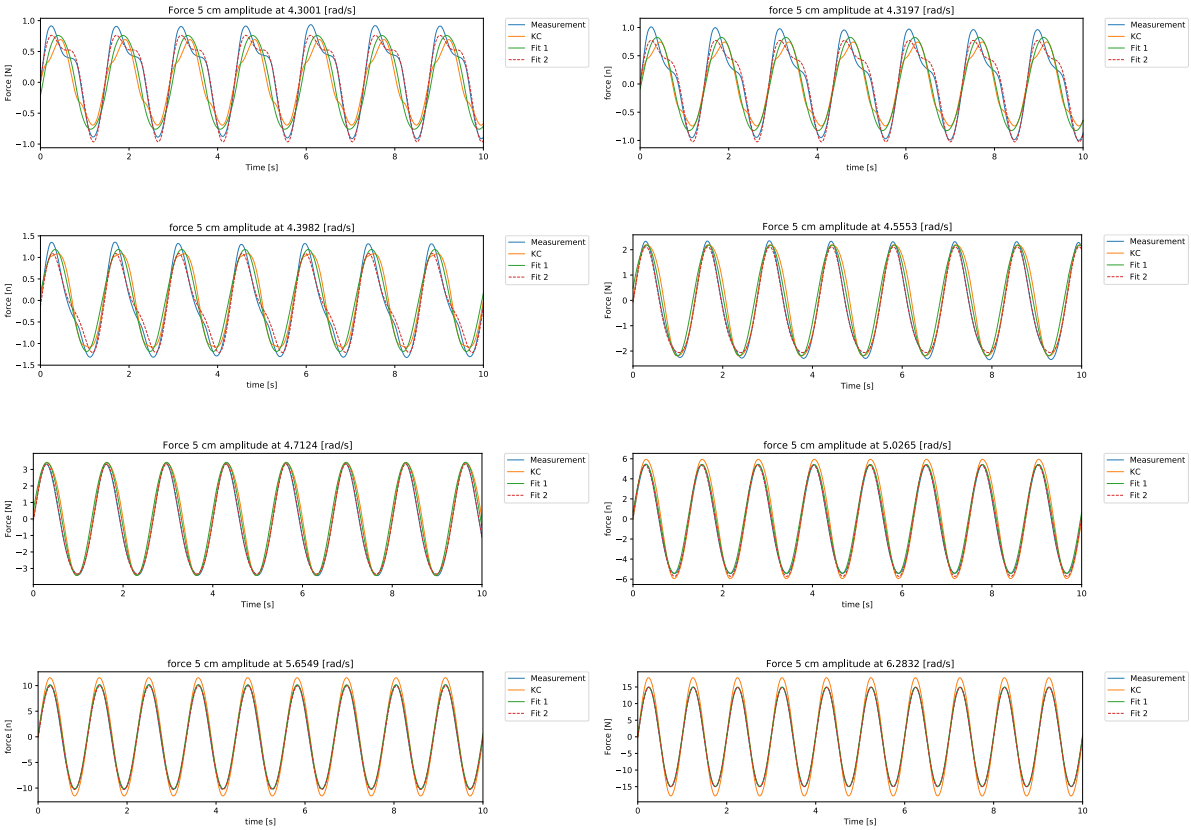
Force 5 cm amplitude at 4.3001 [rad/s]
force 5 cm amplitude at 4.3197 [rad/s]
force 5 cm amplitude at 4.3982 [rad/s]
Force 5 cm amplitude at 4.5553 [rad/s]
Force 5 cm amplitude at 4.7124 [rad/s]
force 5 cm amplitude at 5.0265 [rad/s]
force 5 cm amplitude at 5.6549 [rad/s]
Force 5 cm amplitude at 6.2832 [rad/s]
Measurement
KC
Fit 1
Fit 2
Force [N]
force [n]
Time [s]
time [s]

Hemisphere

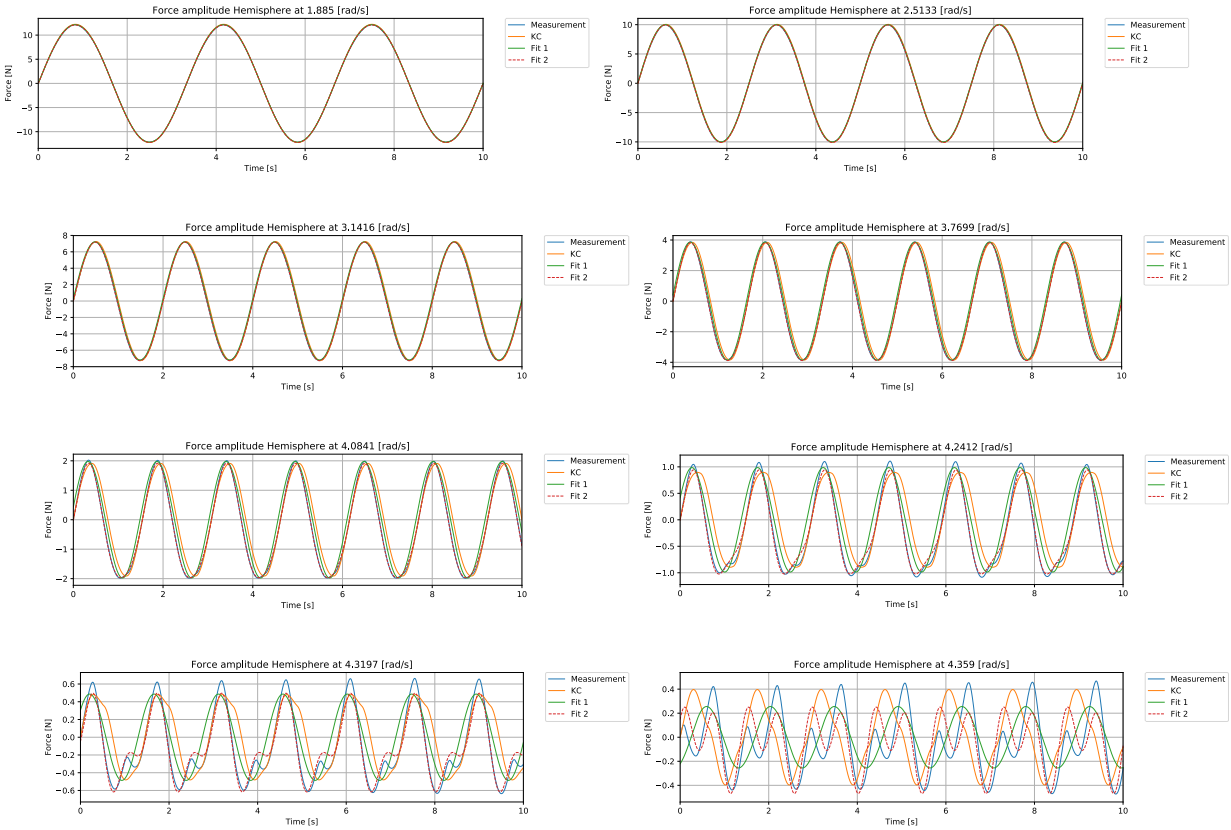
Force amplitude Hemisphere at 1.885 [rad/s]
Force amplitude Hemisphere at 2.5133 [rad/s]
Force amplitude Hemisphere at 3.1416 [rad/s]
Force amplitude Hemisphere at 3.7699 [rad/s]
Force amplitude Hemisphere at 4.0841 [rad/s]
Force amplitude Hemisphere at 4,2412 [rad/s]
Force amplitude Hemisphere at 4.3197 [rad/s]
Force amplitude Hemisphere at 4.359 [rad/s]
Measurement
KC
Fit 1
Fit 2
Force [N]
Time [s]

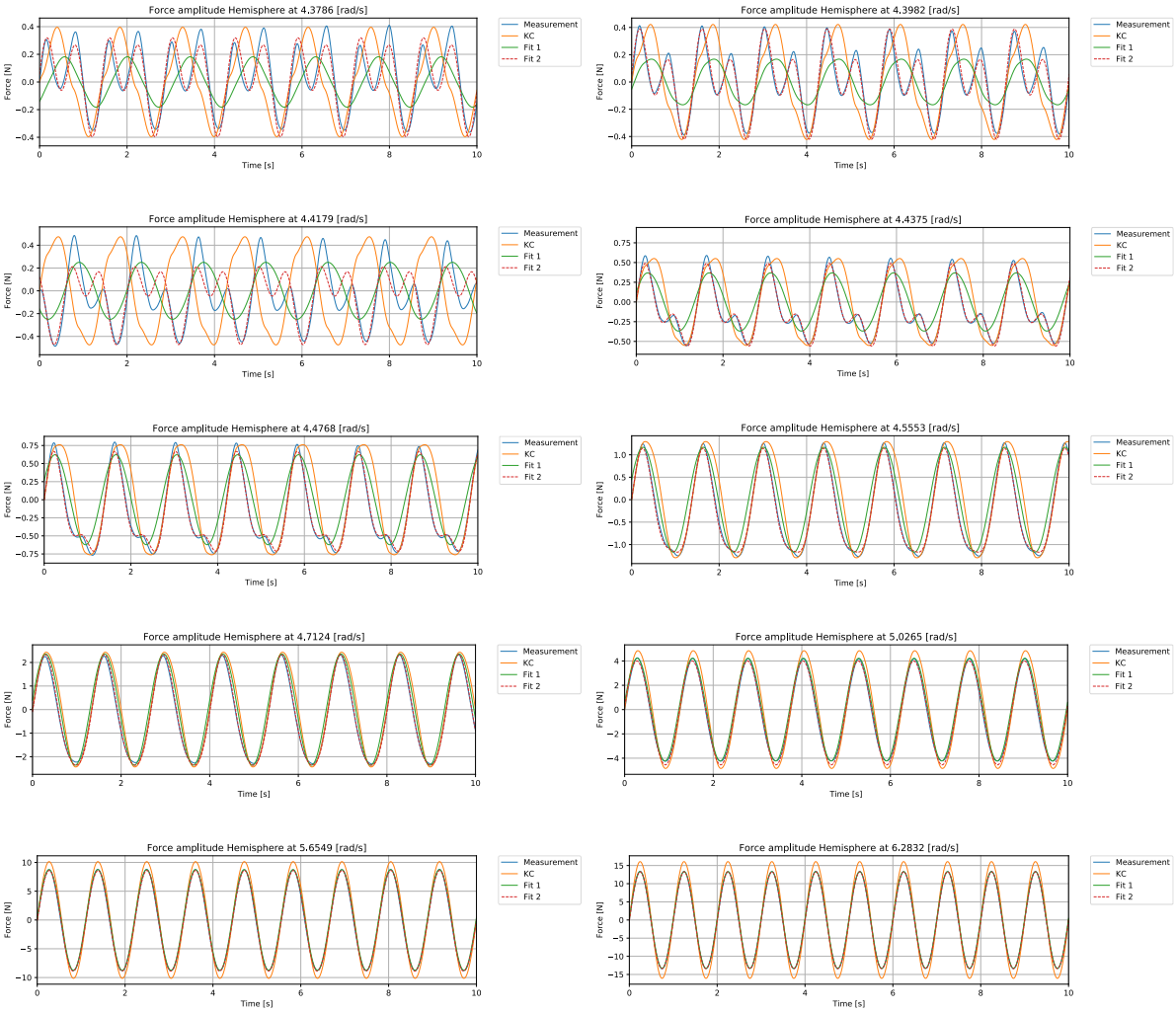
Force amplitude Hemisphere at 4.3786 [rad/s]
Force amplitude Hemisphere at 4.3982 [rad/s]
Force amplitude Hemisphere at 4.4179 [rad/s]
Force amplitude Hemisphere at 4.4375 [rad/s]
Force amplitude Hemisphere at 4.4768 [rad/s]
Force amplitude Hemisphere at 4.5553 [rad/s]
Force amplitude Hemisphere at 4.7124 [rad/s]
Force amplitude Hemisphere at 5.0265 [rad/s]
Force amplitude Hemisphere at 5.6549 [rad/s]
Force amplitude Hemisphere at 6.2832 [rad/s]
Force [N]
Time [s]
Measurement
KC
Fit 1
Fit 2

B

Fit variables

In this appendix the fit variables of methods "Fit 1" and "Fit 2" are illustrated.

Fit 1

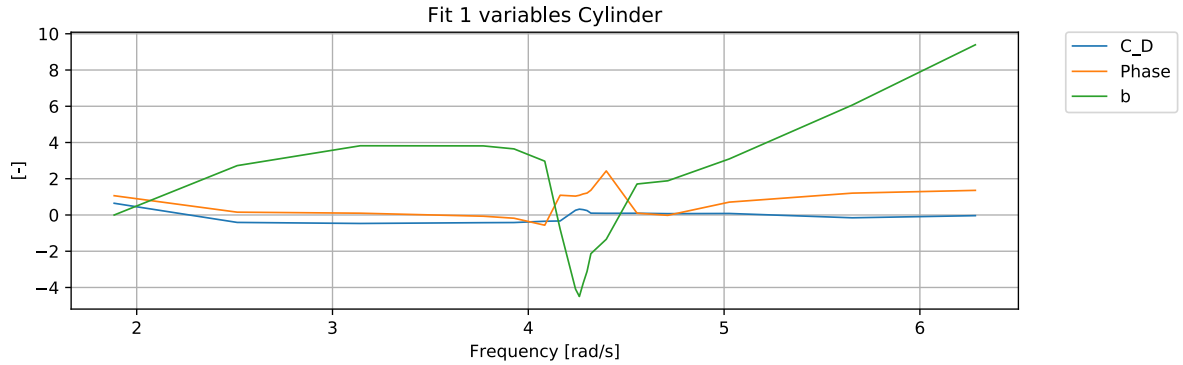

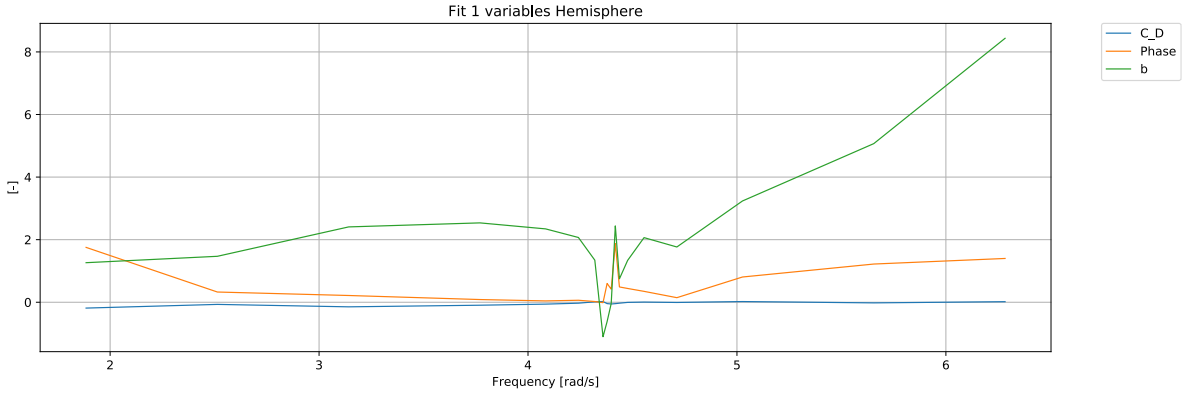

Fit 2

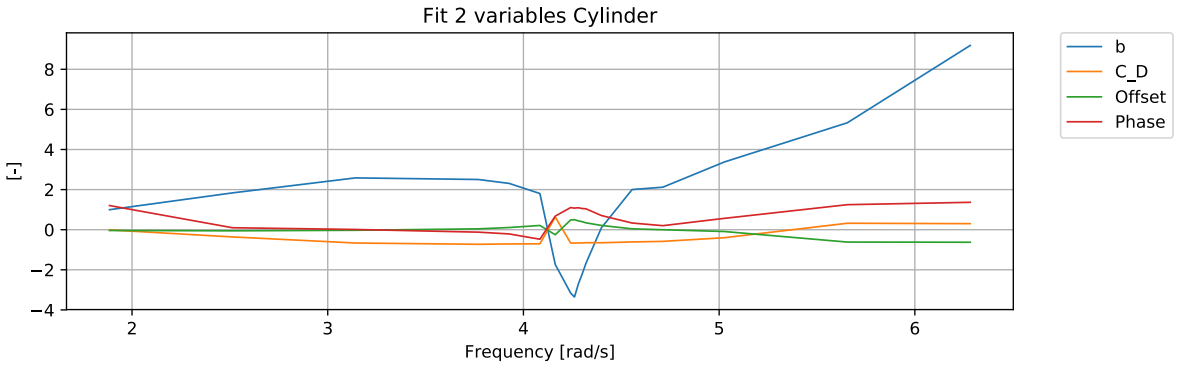
Fit 2 variables Cylinder
[-]
Frequency [rad/s]
b
C_D
Offset
Phase

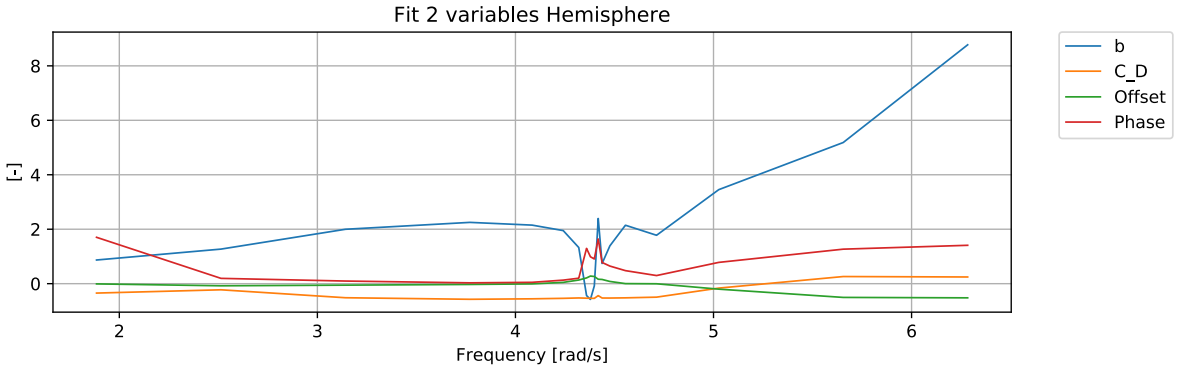
Fit 2 variables Hemisphere
[-]
Frequency [rad/s]
b
C_D
Offset
Phase

Fit 2a

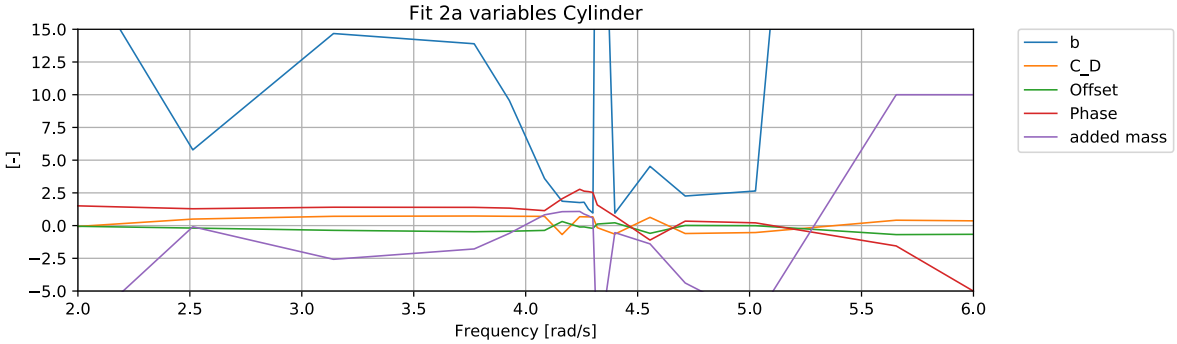
Fit 2a variables Cylinder
[-]
Frequency [rad/s]
b
C_D
Offset
Phase
added mass

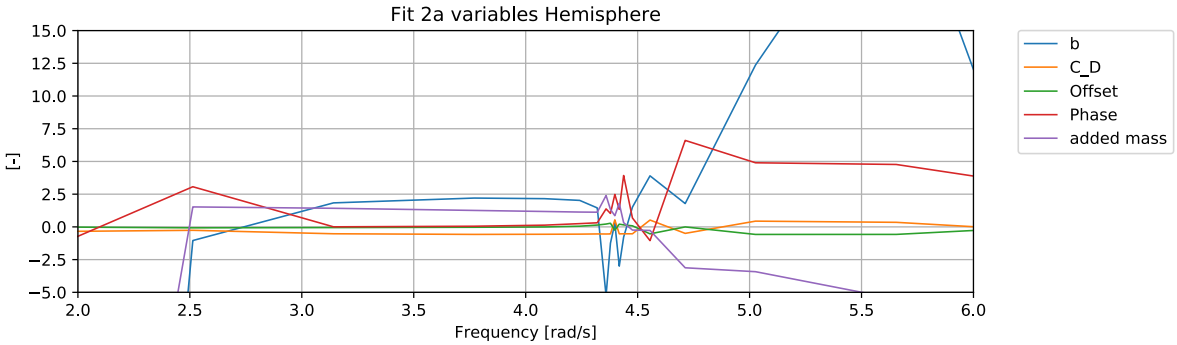
Fit 2a variables Hemisphere
[-]
Frequency [rad/s]
b
C_D
Offset
Phase
added mass

Bibliography

[1] Aurélien Babarit and Gérard Delhommeau. Theoretical and numerical aspects of the open source BEM solver NEMOH. *Proc. 11th Eur. Wave Tidal Energy Conf.*, (September 2015):1–12, 2015. doi: hal-01198800.

[2] Bremerhaven. Status on the Wave Star Energy converter development. 2006.

[3] F. Ferri, M. M. Kramer, and A Pecher. Validation of a wave-body interaction model by experimental tests. 9:500–507, 2013.

[4] General Assembly. Transforming our world: the 2030 Agenda for Sustainable Development. 16301 (October):1–35, 2015. URL `https://generalassemb.ly/design`.

[5] Bingyong Guo and Ron J. Patton. Non-linear Viscous and Friction Effects on a Heaving Point Absorber Dynamics and Latching Control Performance. *IFAC-PapersOnLine*, 50(1):15657–15662, 2017. ISSN 24058963. doi: 10.1016/j.ifacol.2017.08.2394. URL `https://doi.org/10.1016/j.ifacol.2017.08.2394`.

[6] Leo H Holthuijsen, Donald T. Resio, and Joannes J. Westerink. Measurements of Wind-Wave growth and Swell Decay during the Joint North Sea Wave Project. *Coast. Eng.*, 7(1):399–404, 2015. ISSN 03783839. doi: 10.1016/j.coastaleng.2015.09.010. URL `http://dx.doi.org/10.1038/nclimate1979{%}0Ahttp://dx.doi.org/10.1016/j.coastaleng.2016.06.001{%}0Ahttp://www.e3s-conferences.org/10.1051/e3sconf/20160713014{%}0Ahttp://ascelibrary.org/doi/10.1061/{%}28ASCE{%}290733-9429{%}282005{%}29131{%}3A6{%}28497{%}29{%}0Ahttp://dx.doi.org`.

[7] J M J Journée and W W Massie. OFFSHORE HYDROMECHANICS Second Edition (2008) Delft University of Technology. 2008.

[8] Garbis H Keulegan and Lloyd H Carpenter. Forces on Cylinders and Plates in an Oscillating Fluid. (5), 1958.

[9] Sung-Jae Kim, Weoncheol Koo, and Min-Jae Shin. Numerical and experimental study on a hemispheric point-absorber-type wave energy converter with a hydraulic power take-off system. *Renew. Energy*, 135: 1260–1269, 2018. ISSN 09601481. doi: 10.1016/j.renene.2018.09.097. URL `https://doi.org/10.1016/j.renene.2018.09.097`.

[10] T. Kloss, S. Stobiac, and K. Mikhail. Salome, 2001.

[11] MIT. MIT lecture - Wave Forces on body. 2004.

[12] Made Jaya Muliawan, Madjid Karimirad, Torgeir Moan, and Zhen Gao. Omae2012-8 Turbine and Large Point Absorber Floating Wave Energy Converter –. *Omae*, pages 1–10, 2012.

[13] Made Jaya Muliawan, Madjid Karimirad, Zhen Gao, and Torgeir Moan. Extreme responses of a combined spar-type floating wind turbine and floating wave energy converter (STC) system with survival modes. *Ocean Eng.*, 65:71–82, 2013. ISSN 00298018. doi: 10.1016/j.oceaneng.2013.03.002.

[14] Made Jaya Muliawan, Madjid Karimirad, and Torgeir Moan. Dynamic response and power performance of a combined Spar-type floating wind turbine and coaxial floating wave energy converter. *Renew. Energy*, 50:47–57, 2013. ISSN 09601481. doi: 10.1016/j.renene.2012.05.025. URL `http://dx.doi.org/10.1016/j.renene.2012.05.025`.

[15] Court of audit Netherlands. Focus on the cost of offshore wind energy. Technical Report september, 2018.

[16] M Penalba, T Kelly, and J Ringwood. Using NEMOH for modelling wave energy converters: A comparative study with WAMIT. *{P}roceedings of the {T}welfth {E}uropean {W}ave and {T}idal {E}nergy {C}onference*, pages {631\hyphen 1}—-{631\hyphen 10}, 2017.

[17] T Van Riet. Feasibility of ocean energy and offshore wind hybrid solutions. Technical report, TU Delft, 2017.

[18] T. Sarpkaya and M. Storm. In-line force on a cylinder translating in oscillatory flow. *Appl. Ocean Res.*, 7 (4):188–196, 1985. ISSN 01411187. doi: 10.1016/0141-1187(85)90025-2.

[19] Ntnu Grafisk Senter. Arctic and Marine. 2016.

[20] Norio Tanaka, Yoshio Ikeda, and Kimio Nishino. Hydrodynamic viscous force acting on oscillating cylinders with various shapes. *6th Symp. Mar. Technol. Soc. Nav. Archit. Japan*, 1982.

[21] Ling Wan, Zhen Gao, and Torgeir Moan. Experimental and numerical study of hydrodynamic responses of a combined wind and wave energy converter concept in survival modes. *Coast. Eng.*, 104:151–169, 2015. ISSN 03783839. doi: 10.1016/j.coastaleng.2015.07.001. URL `http://dx.doi.org/10.1016/j.coastaleng.2015.07.001`.

[22] P. Wellens. Wave Energy. Technical report, Technical University Delft, 2004.

[23] A. S. Zurkinden, F. Ferri, S. Beatty, J. P. Kofoed, and M. M. Kramer. Non-linear numerical modeling and experimental testing of a point absorber wave energy converter. *Ocean Eng.*, 78:11–21, 2014. ISSN 00298018. doi: 10.1016/j.oceaneng.2013.12.009. URL `http://dx.doi.org/10.1016/j.oceaneng.2013.12.009`.